Materials Science & Engineering R 160 (2024) 100824

Contents lists available at ScienceDirect

Materials Science & Engineering R

journal homepage: www.elsevier.com/locate/mser

Triterpenoid saponin-based supramolecular host-guest injectable hydrogels inhibit the growth of melanoma via ROS-mediated apoptosis

Ramya Mathiyalagan [a,1], Mohananpriya Murugesan [a,1], Zelika Mega Ramadhania [a], Jinnatun Nahar [a], Panchanathan Manivasaga [d], Vinothini Boopathi [a], Eue-Soon Jang [d], Deok Chun Yang [a,b], João Conde [c,*], Thavasyappan Thambi [a,*]

[a] Graduate School of Biotechnology, College of Life Sciences, Kyung Hee University, Yongin si, Gyeonggi do 17104, Republic of Korea
[b] Department of Oriental Medicinal Biotechnology, College of Life Science, Kyung Hee University, Yongin-si, Gyeonggi-do 17104, Republic of Korea
[c] ToxOmics, NOVA Medical School, Faculdade de Ciências Médicas, NMS|FCM, Universidade NOVA de Lisboa, Lisboa, Portugal
[d] Department of Applied Chemistry, Kumoh National Institute of Technology, Daehak-ro 61, Gumi, Gyeongbuk 39177, Republic of Korea

ARTICLE INFO

Keywords:
Cancer nanomedicine
Hydrogels
Melanoma
In vivo
Host-guest biomaterials
Apoptosis

ABSTRACT

Triterpenoids are natural bioactive compounds that demonstrate cytotoxic and chemopreventive activities by inhibiting various intracellular signals and transcription factors. Despite their efficacy, triterpenoid chemotherapeutics face significant challenges in cancer therapy because of their poor aqueous solubility, which restricts the utilization of potent drug variants. Consequently, there is a pressing need to develop a solubilized form of triterpenoid encapsulated within mechanically robust biomaterials, to facilitate injectable and minimally invasive delivery. In this study, we focused on ginsenoside compound K (CK), a natural pentacyclic triterpenoid. It was conjugated to hyaluronic acid (HA-CK) and employed as a novel guest molecule for binding to β-cyclodextrin-grafted hyaluronic acid (HA-βCD), which is the host polymer. This interaction resulted in the creation of an injectable supramolecular hydrogel (HG-Gel) through a straightforward mixing process involving host–guest interactions between βCD and CK. The physical properties of the hydrogels were easily manipulated by altering the molecular weight of HA and the grafting degree of βCD and CK in HA. Notably, the supramolecular hydrogel precursors exhibited excellent cell viability for normal cells, sparing over 80 % of NIH 3T3 and HaCaT cells. Intriguingly, these hydrogels facilitated effective delivery to CD44-overexpressing cancer cells, suppressing cell proliferation. Enhanced trafficking of CK to cancer cells heightened caspase-dependent apoptosis in B16F10 cells, with the extent of cell death contingent on the expression levels of CD44 in cancer cells. This effect of CK seems to be mediated through the induction of intracellular reactive oxygen species (ROS) and mitochondrial membrane potential loss. In melanoma tumor-bearing mouse models, HG-Gels effectively inhibited tumor growth. Importantly, no side effects were observed on normal tissues, underscoring the safety of naturally derived biomaterials. This study underscores the superiority of HG-Gels as a platform for utilizing triterpenoid saponins in melanoma therapy, suggesting their potential for enhancing the safety and efficacy of triterpenoids in cancer treatment.

1. Introduction

Injectable materials, often in the form of hydrogels [1], can be introduced into tissues through percutaneous procedures using syringes and catheters, finding widespread applications in various biomedical fields [2]. Traditionally, these materials are isotropic and homogeneous, typically incorporating a blend of natural and synthetic polymers to govern their physiological responsiveness [3]. While covalently crosslinked hydrogels boast numerous advantages, they tend to be brittle, and supramolecular assemblies often exhibit pseudoplastic deformation with low resistance to loading [4]. Within this realm, self-assembled hydrogels stand out as a specific category, utilizing crosslinking chemistry derived from noncovalent interactions such as hydrophobic [5], ionic [6], and guest–host binding [7,8]. Notably, these materials often possess shear-thinning properties [9], allowing for easy injection and subsequent stabilization upon reaching the injection site

* Corresponding authors.
E-mail addresses: joao.conde@nms.unl.pt (J. Conde), thambi@khu.ac.kr (T. Thambi).
[1] These authors contributed equally to this work.

https://doi.org/10.1016/j.mser.2024.100824
Received 27 March 2024; Received in revised form 20 June 2024; Accepted 2 July 2024
Available online 17 July 2024

[10].

Various non-covalent interactions can induce the formation of shear-thinning hydrogels [11]. However, many of these interactions suffer from the drawbacks of non-specificity and harsh gel formation conditions, ultimately constraining the broader applications of hydrogels. To address these limitations, researchers have delved into exploring host–guest interactions involving two molecules with non-covalent bonds [12]. Supramolecular chemistries based on host-guest interactions, such as β-cyclodextrin-Paclitaxel [13], Cucurbit-Temozolomide [14], and Calixarene-Ciprofloxacin [15], present an appealing avenue for designing injectable hydrogels. These chemistries not only facilitate shear-thinning behavior but also offer the advantage of fine-tuning viscoelastic mechanical properties through both primary and secondary cross-linking mechanisms, overcoming the challenges posed by non-specificity and demanding gel formation conditions.

β-cyclodextrin (βCD), a cyclic oligosaccharide comprising seven glucopyranose units, features a distinctive structure with a hydrophilic outer cavity and a hydrophobic inner cavity [16]. This cyclodextrin, recognized as non-toxic by the U.S. Food and Drug Administration, enjoys widespread use in diverse industries, including food, cosmetics, and pharmaceuticals [17]. Its ability to encapsulate guest molecules within its cavity makes it a typical host molecule [18]. Paclitaxel (PTX), an agent known to stabilize microtubules and reduce their dynamicity, thereby promoting mitotic arrest and cell death [19], stands out as an ideal guest molecule. Its suitable molecular volume, hydrophobic properties, and relatively high association constant with βCD make it a compelling candidate [20]. The host–guest interaction between βCD and PTX has garnered increasing attention for the development of functional biomaterials [21]. Guest−host assembled hydrogels, owing to their non-Newtonian properties, are well-suited as cell carriers for injectable delivery, offering protection against excessive shear during needle extrusion [22]. Despite these advantages, achieving fibrillar topographies in mechanically robust injectable hydrogels remains challenging. Although self-assembling peptides can serve as injectable nanofibrous hydrogels [23], their long-term mechanical properties are often limited. On the other hand, electrospun hydrogel materials, exhibit robust mechanics and support biomimetic cellular behaviors. However, these scaffolds typically require physical implantation and are not amenable to injectable delivery.

Triterpenoids, a class of naturally occurring bioactive compounds, are abundantly present in various plants as free acids or aglycones [24]. They constitute one of the largest subclasses of specialized metabolites, encompassing over 14,000 known structures [25]. Based on their structures, triterpenoids are divided into different subgroups, such as acyclic and cyclic compounds [26]. Major types include tetracyclic derivatives, such as dammarane, cucurbitane, tirucallane, and euphane. Dammarane triterpenoids, the main metabolites of Panax ginseng, are particularly important due to their remarkable biological activity [27]. Typically composed of six isoprene units, these triterpenoids exhibit multiple functional groups, unique chiral centers, rigid skeletons, and excellent biocompatibility [28]. These distinctive attributes not only confer their pharmacological properties but also make them ideal building blocks for self-assembling versatile supramolecular structures. However, many of these compounds, including 293 isolated ginsenosides, exhibit poor solubility and targetability. To overcome challenges related to solubility and non-targetability, pentacyclic triterpenoid-based small molecules have frequently been incorporated into micro or nanoparticles [28]. However, the application of these low-molecular-weight gels is limited, either because of the use of toxic organic solvents or their poor mechanical properties. Hence, there is a need to explore the development of polymeric hydrogels based on pentacyclic triterpenoids, potentially opening up new possibilities in the field of biomaterials derived from these compounds.

To address the poor solubility of triterpenoids, resulting in a brief half-life in the blood circulation, low bioavailability, and limited therapeutic effectiveness, a strategy was devised to chemically conjugate triterpenoids to the hyaluronic acid (HA) backbone. In this study, ginsenoside compound K (CK) was selected as the representative drug candidate, considering that dammarane-based triterpenoids, after intravenous administration, often undergo non-specific distribution in the body, especially in low-molecular-weight variants. To create a supramolecular hydrogel, a conjugate of HA and βCD was synthesized using natural resources. Both conjugates formed a complex through host-guest interactions, with CK and βCD groups facilitating a dynamic network characterized by reversible interactions within physiological conditions. This approach effectively addressed the issues associated with most dammarane-based triterpenoids. A similar approach can be used by substituting CK with other ginsenosides, and the resulting conjugate or gel can be used for various biomedical applications. The resulting hydrogel exhibited excellent injectability and self-healing properties. Validation in a melanoma tumor model confirmed that the injection of the hydrogel (HG-Gel) achieved precise and sustained release of CK at the tumor site without evident long-term toxicity, thus simplifying the frequency of drug administration. These findings indicate the suitability of hydrogels as effective biomaterials for melanoma treatment. Notably, this work represents the first instance of employing a preassembly approach that combines host-guest interactions with triterpenoids to construct an injectable hydrogel with hydrolytic degradation resistance and multifunctionality. This study introduced a general strategy for preparing triterpenoid-based hydrogels, paving a new avenue for the fabrication of intelligent biomedical materials with promising applications. Fig. 1 illustrates the synthesis route and working principle of injectable supramolecular hydrogels, both in vitro and in vivo.

2. Results and discussion

In our pursuit to construct supramolecular materials using entirely natural polymers derived from plants, animals, and microorganisms—integral components with exceptional properties and vital roles in sustaining life—we posit that pre-organizing the host and guest monomers enhances in-situ gelation efficiency. In this context, we explore the conjugation of host and guest monomers to the backbone of water-soluble and non-immunogenic HA. Our approach involves the synthesis of HA-βCD and HA-CK conjugates, where simple mixing of these conjugates leads to the formation of host-guest inclusion complexes (Fig. 1**a**). These complexes arise through non-covalent crosslinks between βCD and CK, ultimately giving rise to supramolecular hydrogels to apply in a tumor mouse model leading to a ROS-mediated apoptosis mechanism (Fig. 1**c**). This strategy offers a versatile and efficient method for creating hydrogels with desirable properties, aligning with the overarching goal of utilizing natural polymers for innovative materials in various applications.

To create injectable hydrogels based on HA through host-guest interactions, precursor polymers HA-CK and HA-βCD were synthesized, as illustrated in Figure S1, Supporting Information.

Before host-guest complexation, HA-βCD was synthesized as the host polymer through an esterification reaction between βCD and HA (Figure S1a, Supporting Information). Comparative analysis with HA revealed that the ^{1}H NMR spectrum of HA-βCD exhibited new signals corresponding to anomeric protons at 5.2 ppm and the C-6 methylene group[29] attributed to the protons of βCD. This observation affirmed the successful conjugation of βCD into the backbone of HA. The singlet peak of –CH protons in βCD was distinctly present at $\delta = 5.2$ ppm and exhibited a gradual increase with an increasing degree of substitution (DS) of βCD (Fig. 2**a, c**), indicating the successful preparation of HA-βCD (Table S1, Supporting Information). As anticipated, the proton peaks of polysaccharide units in the HA backbone and βCD ring substantially overlapped in the range of $\delta = 3.4$–4.2 ppm. With an increase in the DS of βCD, the peaks corresponding to HA gradually weakened.

Subsequently, the hydrophobic guest monomer CK, which is insoluble in water, was conjugated to the HA backbone through carbonyl

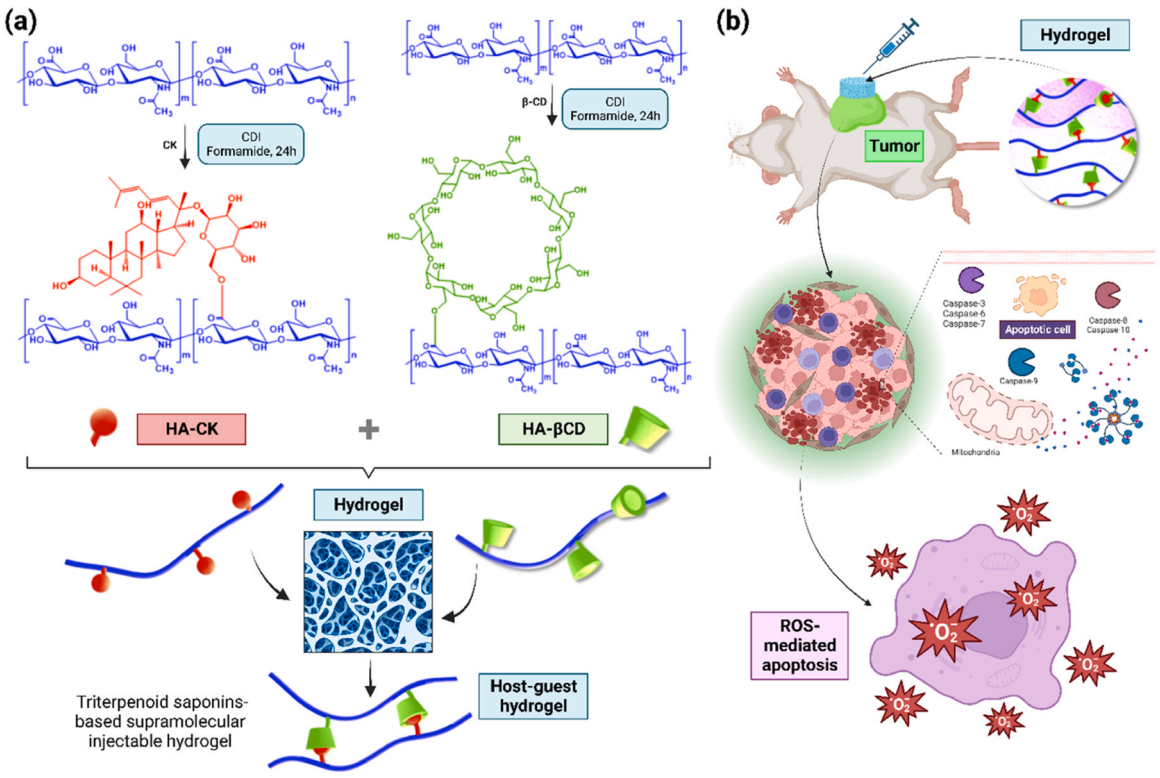

Fig. 1. Schematic illustration of an injectable supramolecular hydrogel and mechanism of injectable hydrogel system that exerts anticancer efficacy in the treatment of advanced melanoma through induction of ROS-mediated apoptosis by cleavage of caspases-9 and −3. (a) Preparation of an injectable supramolecular hydrogel using HA-βCD and HA-CK conjugates. The βCD and CK units in the backbone of HA could form inclusion complexes due to the formation of hydrogen bonds in the hydrophobic interior of βCD and CK, thereby forming a supramolecular hydrogel. (b) The mechanism of the supramolecular hydrogel triggered anticancer effect in a melanoma tumor model after subcutaneous injection.

diimidazole (CDI)-mediated esterification, resulting in the HA-CK conjugate (Figure S1b, Supporting Information). This method not only enhanced CK solubility but also reduced toxicity to normal cells and improved target specificity to tumor cells [30]. The ^{1}H NMR characterization confirmed the successful grafting of CK onto the HA chains, with the degree of substitution varying based on the molecular weight of HA (Fig. 2**b, d**). Specifically, the degree of substitution decreased with increasing HA molecular weight (Table S2, Supporting Information). Importantly, the substitution efficiency exhibited a notable decrease with the higher molecular weight of HA, possibly attributed to an apparent steric hindrance effect caused by the elongated polymer chain [31].

Fourier-transform infrared (FT-IR) spectroscopy proves to be a valuable method for scrutinizing alterations in the chemical bonds of substances. In the FT-IR spectrum of HA (Fig. 2**e, f**), the antisymmetric and symmetric stretching vibration absorption peaks of carboxylate groups were prominently observed at 1640 and 1417 cm^{-1}, respectively [32]. Following the grafting of βCD to HA, the intensity of the broad trough corresponding to the OH bond and the –COOH characteristic peak diminished. Notably, an additional small peak emerged at 1740 cm^{-1}, attributed to the C═O stretching vibration in ester groups (–COO^{-}), signifying the conversion of part of –COOH in HA to –COO^{-} in HA-βCD. To highlight these ester bonds more clearly, the diagnostic regions were enlarged as shown in Figure S2 (Supporting Information). These alterations in characteristic peaks provided clear evidence of the successful conjugation of βCD to HA chains. In the FT-IR spectra of HA-CK conjugates, alongside the major characteristic peaks of HA, vibration bands corresponding to the C−O, C−H, and C−OH groups appeared at 1645, 1401, and 1069 cm^{-1}, respectively. Importantly, the intensity of the ester peaks gradually intensified with increasing degree of substitution (DS), underscoring successful conjugation.

To prepare supramolecular injectable HA-based hydrogels, HA-βCD and HA-CK conjugates with different molar ratios [βCD:CK = 1:1, 1:2, 1:3, 2:1, 2:2; 2:3] were dispersed in PBS for 6 hours at 40 °C. The HA-βCD conjugates resulted in a transparent solution owing to the presence of water-soluble polysaccharides (Fig. 3a (Figure S3, Supporting Information)). In contrast, the HA-CK did not exhibit a transparent solution due to the hydrophobic nature of CK. As illustrated in Fig. 3**a**, HG-Gels were created by mixing HA-βCD and HA-CK under physiological conditions. Gelation was confirmed using a rheological test (Figure S4, Supporting Information). The mixed solutions were transformed into supramolecular hydrogels within seconds or minutes, depending on the molar ratio of βCD: CK. The gelation mechanism of the HG-Gels was attributed to the formation of a hydrophobic complex through supramolecular host-guest interactions. Importantly, the preassembled precursor polymers significantly accelerated the assembly efficiency, circumventing the less efficient supramolecular assembly achieved by directly mixing the modified polymers. To validate the structure of the HG-Gels, they were freeze-dried and characterized using XRD and DSC spectroscopy.

The formation of the inclusion complex based on the host-guest interaction between βCD and CK was validated through XRD. In the presented Fig. 3**b**, both HA and CK appeared in an amorphous state without discernible diffraction, while βCD exhibited multiple strong crystal diffraction peaks in the range of 5°-30° [33]. Notably, the XRD patterns of HG-Gels differed significantly from those of pure HA, βCD, and CK. A distinct and robust characteristic diffraction peak at 2θ = 34.7° was evident in the XRD patterns of HG-Gels. This characteristic peak in the crystalline structure confirmed the formation of the inclusion complex, signifying that the dammarane structure of CK penetrated the βCD cavity to create an inclusion complex structure. This formation was facilitated by the hydrophobic inner cavity of βCD and the hydrophobic

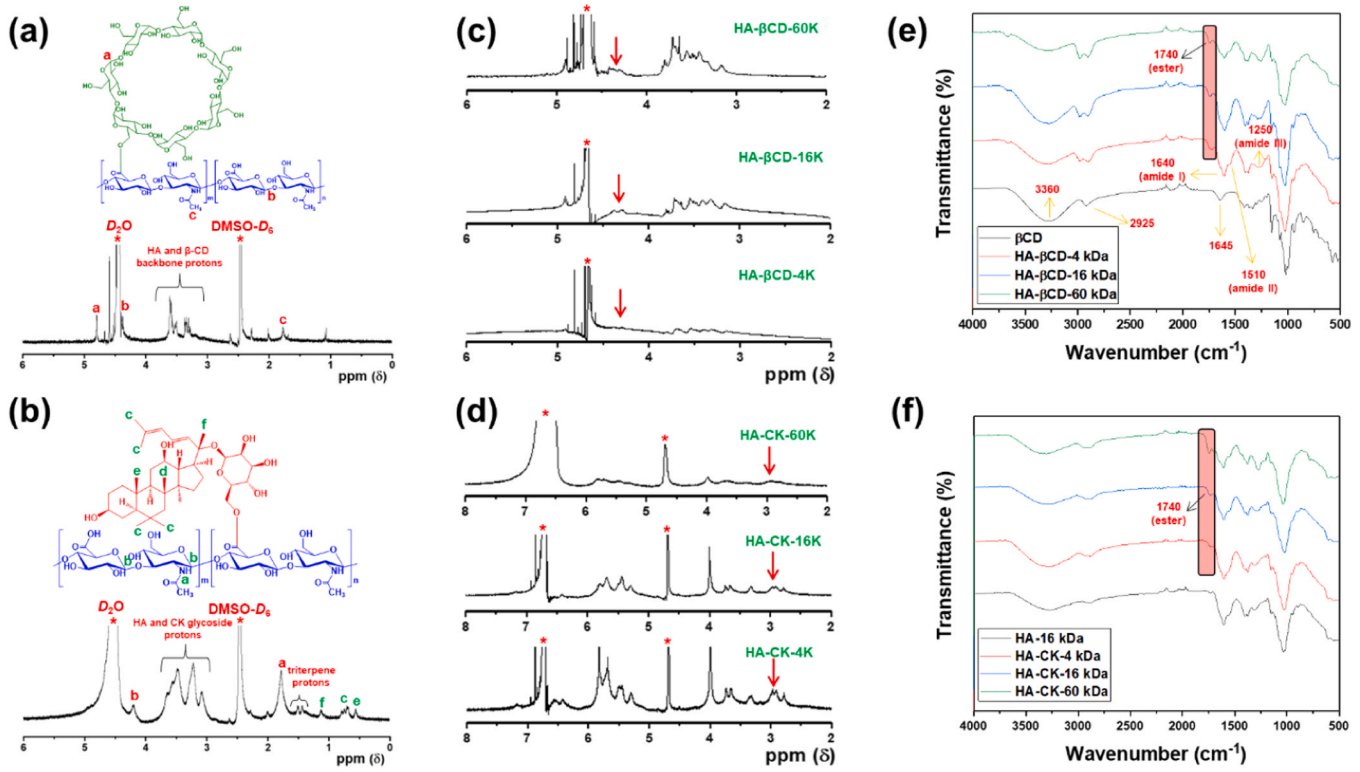

Fig. 2. Characterizations of the HA-βCD and HA-CK conjugates. (a and c) ^{1}H NMR spectra of HA-βCD conjugates. (b and d) ^{1}H NMR spectra of HA-CK conjugates. Asterisks (*) denote the residual solvent peaks. Red arrows indicate corresponding increase in the βCD and CK conjugates in the conjugates with respect to the decrease in the molecular weight of HA. (e and f) FTIR spectra of HA-βCD and HA-CK conjugates. The orange-brown band highlights the presence of ester linkages in the conjugates, which confirmed the effective conjugation of βCD and CK to the HA.

pentacyclic rings.

To further explore the interaction between βCD and CK, a DSC study was performed **(**Fig. 3**c)**. Analysis of the heating curves of native compounds and HA conjugates alone or in combination allowed us to identify interactions between host and guest molecules due to complex formation. The DSC thermogram of βCD showed two broad peaks at 82.6 and 330.1 °C, corresponding to the loss of water absorbed in the inner cavity and its melting point, respectively [34]. This observation is consistent with previously reported DSC thermograms of βCD. For native HA, a sharp characteristic peak was observed at 231 °C, which corresponded to the thermal decomposition of HA. For instance, Pan et al. reported a similar thermal degradation pattern for HA [35]. In contrast, for HA-βCD conjugates, the characteristic melting peaks of βCD and the decomposition peaks of HA disappeared, indicating the effective conjugation of βCD to the backbone of HA through ester bond formation. A similar change in the DSC curve pattern for modified βCD has been reported for citrate derivatives of βCD, where the melting point peak of βCD disappeared [36].

For the HG-Gels, the characteristic melting peak of βCD completely disappeared in the DSC thermogram, indicating that CK was embedded into the non-polar cavity of βCD, forming an amorphous complex. Additionally, the change in the molecular weights of HA and βCD in the HG-Gels did not alter the formation of the host-guest complex. A similar pattern was observed for the host-guest complexes prepared using βCD and its derivatives. DSC analysis of the different HG-Gels provided strong evidence of physical changes and suggested the formation of inclusion complexes. The disappearance of the thermal peaks of the host molecules further indicated the successful formation of the host-guest complex.

2.1. *Thermal properties of HG-Gels*

Thermogravimetric analysis (TGA) is a commonly employed technique for analyzing the thermal stability of polymers and their derivatives (Fig. 3**d**)[37]. TGA provides information about the thermal decomposition pattern; therefore, the thermal stability and decomposition of native HA, βCD, HA-βCD, and three different HG-Gels were investigated using this technique. The TGA curves in Fig. 3d were obtained by plotting the percentage weight loss of the polymers versus temperature. The TGA curve of βCD shows a two-step weight loss: the first loss observed between 34 and 82 °C is due to the loss of water molecules in the inner cavity of βCD, and the second weight loss at 380 °C is due to the decomposition of the sample, with residual weight dropping to less than 10 %. The weight loss pattern of βCD observed in this study is consistent with previously reported studies [38]. The TGA curve of HA showed multiple weight loss stages. The first major weight loss occurred at 80 °C, which was likely due to the loss of bound and/or H-bonded water molecules within the natural polymer. A sharp reduction in weight loss was observed at 278 °C owing to the decomposition of natural HA. The residual weight of HA is approximately 38 % at 500 °C [39].

For the HA-βCD conjugate, the degradation curve shifted to a slightly higher temperature than that of native HA, indicating increased thermal stability owing to the formation of covalent bonds between HA and βCD. During the thermal decomposition of HG-Gels, the decomposition rate decreased over a broader range of 210–500 °C, potentially influenced by the formation of inclusion complexes that could mitigate the decomposition of the HA repeating units. In the HG-Gels, water evaporation primarily occurs in the initial stage of thermal decomposition (<120 °C), while the later stage of weight loss predominantly results from the decomposition and loss of functional groups at higher temperatures. Notably, HG-Gels, which had a slightly lower initial decomposition

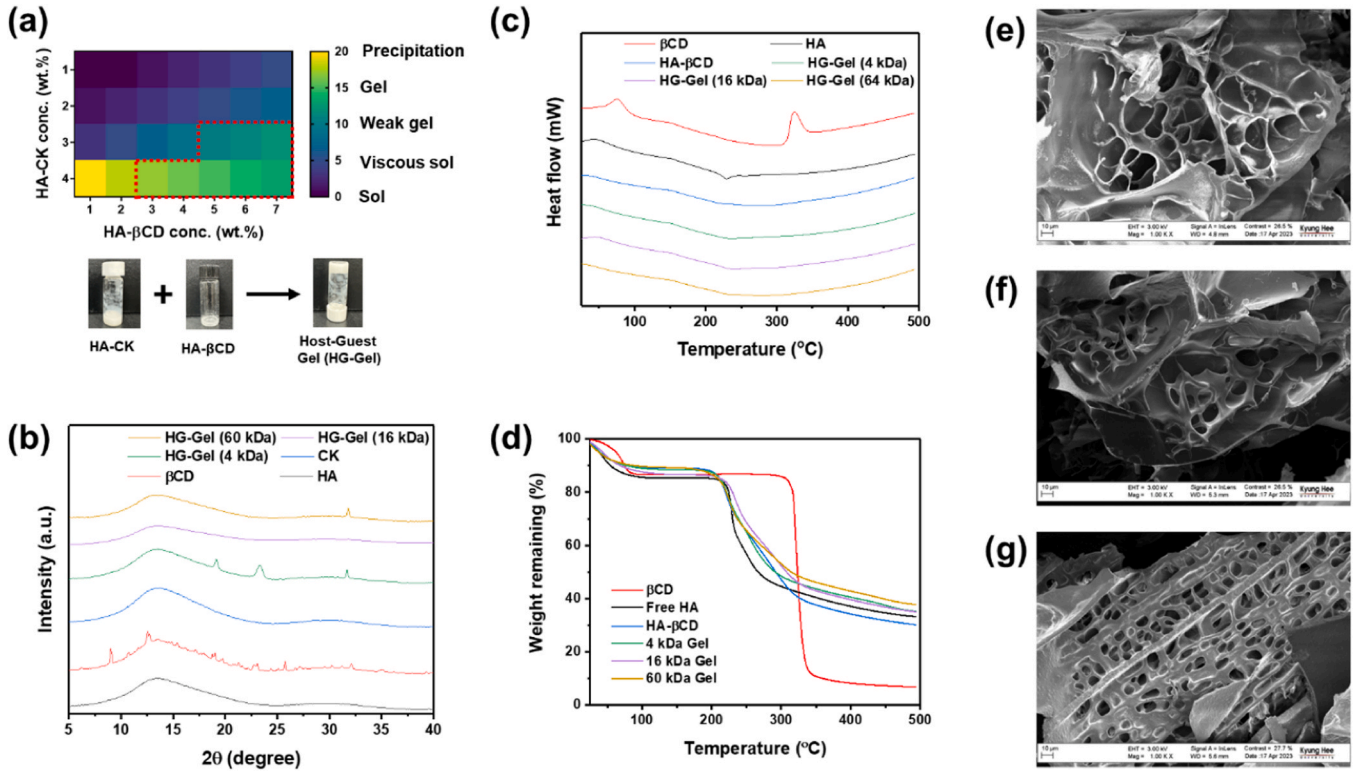

Fig. 3. The properties of HG-Gels. (a) A two-dimensional contour map depicting gelation with varying mixing ratios of host (HA-βCD) and guest (HA-CK) conjugates is presented. The stable gel-forming area is highlighted by red dotted points. A corresponding photograph illustrates the dispersion of HA-βCD and HA-CK conjugates in PBS. Upon mixing, the system undergoes gelation, as visually evidenced in the image. (b) XRD patterns of HA, βCD, CK, and HG-Gels prepared with different molecular weight HA. (c) DSC spectra of HA, βCD, HA-βCD, and HG-Gels prepared with different molecular weight HA. (d) TGA curves of HA, βCD, HA-βCD, and HG-Gels prepared with different molecular weight HA. (e-g) FE-SEM images of surface micromorphology of the HG-Gels after lyophilization prepared with varying molecular weight of HA.

temperature, underwent a slower thermal decomposition process. This is likely attributed to the formation of a robust inclusion complex and strong hydrophobic interactions between βCD and CK. Additionally, molecular entanglements forming macromolecular chains stabilized by hydrogen bonds can influence the thermal stability of the biomaterials [40].

2.2. Morphology of HG-Gels

FE-SEM analysis unveiled a porous 3D microstructure of freeze-dried HG-Gels. Notably, as the molecular weight of the host and guest molecules in the polymers increased, discernible differences in density and wall thickness, particularly in the internal morphology, were observed. HG-Gel-4 kDa exhibited a loose lamellar structure with layers connected in a sparse network (Fig. 3**e**), while HG-Gel-16 kDa displayed a compact and uniform circular hole-like structure (Fig. 3**f**). Remarkably, HG-Gel-60 kDa exhibited a distinctive honeycomb-like structure (Fig. 3**g**). The increase in the molecular weight of HA in the βCD and CK conjugates increased the degree of cross-linking of the host and guest polymers, resulting in a transformation of the micromorphology from a loose macro-porous network to a dense porous structure. In terms of surface morphology, all hydrogels displayed similar honeycomb-like porous structures, yet HG-Gel-4 kDa had a looser structure, smaller diameter, and higher density of pores compared to HG-Gel-60 kDa. The significant differences between the surface and internal structures of HG-Gel-4 kDa and HG-Gel-60 kDa may be attributed to the greater susceptibility of low cross-linking hydrogels to environmental influences during formation and freeze-drying processes. In contrast, HG-Gel-16 kDa exhibited consistency between surface and internal structures, indicating effective resistance to such influences owing to a higher cross-linking degree. These differences in micromorphology imply that hydrogels with low cross-linking have inferior mechanical properties. However, the porous 3D structure observed was beneficial for the transport of nutrients and metabolites to cells encapsulated within the hydrogels.

2.3. In vitro release of CK from HG-Gels

In general, hydroxyl groups of various chemotherapeutic drugs, including paclitaxel or docetaxel, are often directly conjugated to the carboxylic groups of HA through ester bond formation, an acid-labile linkage [41]. These conjugated drugs exhibit drug release by hydrolysis under acidic pH conditions, exploiting the tumor microenvironment's acidic pH (6.0–7.0) compared with normal plasma (7.4). Additionally, lysosomes, which are cell organelles that digest engulfed foreign particles, have a pH of 4.0–5.0, facilitating the rapid release of drugs inside the cells. Similarly, various studies have developed cisplatin-conjugated PEG polymers via ester bonds, showing a pH-dependent drug release pattern [42].

In this study, we developed HA-CK conjugates by attaching CK to the backbone of HA through ester bond formation (Fig. 1). The HA-CK conjugates form a complex with HA-βCD conjugates through host-guest interactions between βCD (host) and CK (guest), resulting in a gel depot called HG-Gels. The stability and mechanical properties of the hydrogels at human body temperature were confirmed by incubating the HG-Gels under physiological conditions (pH 7.4, 37 °C) (Figure S5, Supporting Information). Stability testing of HG-Gels confirmed that hydrogels are stable at pH 7.4 and can be a suitable formulation for subcutaneous implantation. Furthermore, the compression test confirmed the gradual increase in mechanical toughness with increasing molecular weight of the HG-Gels (Figure S6, Supporting Information).

Upon subcutaneous implantation, HG-Gels exhibit controlled disassembly of the host-guest interaction and begin releasing independent HA-CK conjugates. These conjugates are taken up by surrounding cancer cells via CD44-dependent uptake and release of CK under intracellular enzyme and acidic pH conditions. The release mechanism of CK is illustrated in Figure S7 (Supporting Information). To examine the release rates of CK from hydrogels under clinically relevant conditions, we conducted release experiments in which HG-Gels were incubated under physiologically relevant pH conditions (pH 7.4) at 37°C. The release of CK was monitored over time. As depicted in Figure S8 (Supporting Information), CK release from HG-Gels was sustained, with approximately 44 % of the drug released in 7 days.

2.4. Hemocompatibility and cytocompatibility analysis

The Fig. 4**a** illustrates the hemocompatibility evaluation of the HG-Gels and its precursors. The hemolysis ratio and erythrocyte durability were employed to assess the hemocompatibility of the hydrogel[43]. After 1 hour of incubation, PBS, HA, βCD, and HA-βCD exhibited significantly lower hemolysis ratios (less than 5 %) than Triton-X. No obvious hemolysis was observed in any of the samples. As anticipated, Triton-X induced severe hemolysis of red blood cells within 2 hours. The low hemolysis ratio (less than 5 %) demonstrated that the modification of HA in this study is suitable for clinical applications. Additionally, the microscopic observation of red blood cell (RBC) morphology after treatment with hydrogels revealed that all treated RBCs maintained a biconcave disc shape, resembling the shape of healthy RBCs in the PBS group, except for the Triton-X group (Fig. 4b).

Normal cells (NIH 3T3 and HaCaT) and cancer cells (B16F10) with varying CD44 expression levels, ranging from none to high levels, were employed to assess the toxicity of the HG-Gel precursors. In comparison to the untreated control group, the cell viability of each group remained over 95 % after 48 hours of incubation (Fig. 4c-f, (Figure S9, Supporting Information)). Notably, even at a concentration of 1000 μg, the three different HA-βCD formulations exhibited good cell compatibility. Collectively, these results demonstrate that HG-Gels possess favorable hemocompatibility and cytocompatibility.

2.5. In vitro cytotoxicity of HG-Gels

Furthermore, considering the biocompatibility of HG-Gel hydrogel precursors, an in vitro cytotoxicity assay of HA-CK at different concentrations was conducted to evaluate the efficacy of released CK on CD44-expressing and non-expressing cells (Fig. 5**a-c**). The HA-CK conjugates exhibit no toxicity towards normal cells, including NIH 3T3 and HaCaT cells. This suggests the site-specific nature of the conjugates. Remarkably, the HA-CK conjugates demonstrated dose-dependent toxicity in cancer cells, showing a dependency on the amount of CK conjugation. Notably, the cell viability of HA-CK-4 kDa and HA-CK-16 kDa decreased to 20.13 % and 10.98 %, respectively. In contrast, at the same concentration, the cell viability of HA-CK-60 kDa was 63.02 %. This can be explained by the difference in the molecular weight of HA in the HA-CK shell. The higher molecular weight effectively controlled the dissociation of CK in the conjugation process and required more time, as internalization was delayed in CD44-mediated endocytosis. Subsequently, a Live/Dead assay was employed to assess the effect of HA-CK conjugates (Figs. 5**d and** 5**e**). Fluorescence microscopy images revealed no significant dead cell population compared to the control group and exhibited dose-dependent toxicity for HA-CK conjugates. This highlights the excellent cytocompatibility of the hydrogel and its ability to exhibit toxicity toward cancer cells while sparing normal cells, making it a promising vehicle in the biomedical field.

2.6. Determination of intracellular ROS

ROS levels were determined using the H_2DCFDA staining assay. The generation of ROS by HA-CK conjugates was examined in HaCaT and B16F10 cells, and the results were compared with H_2O_2-induced cells and non-treated cells·H_2O_2 can induce ROS generation in cells, leading to oxidative stress and the activation of multiple signaling pathways

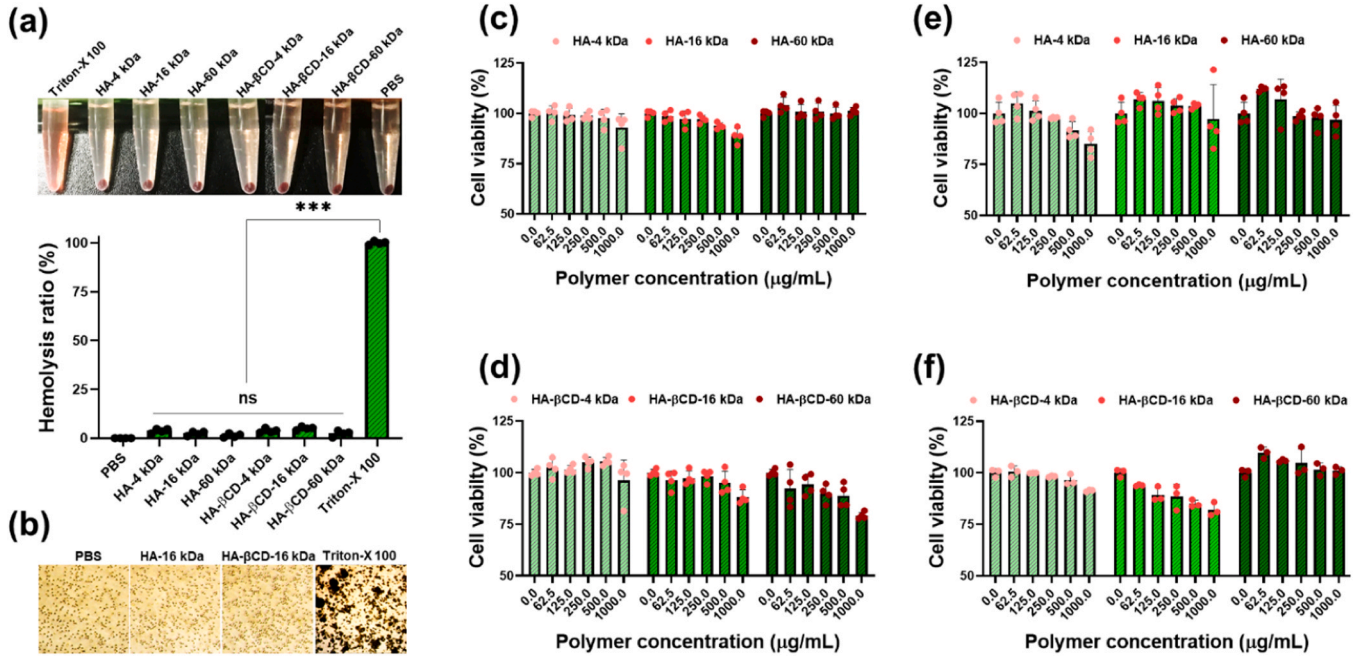

Fig. 4. Hemocompatibility and cytocompatibility of HG-Gel precursors. (a) Optical image and hemolysis ratio of RBCs after incubating with HA and HA-βCD conjugates at 37 °C for 3 h. PBS and Triton-X 100 were used as negative and positive control, respectively. (b) Optical microscopic images of RBCs after incubating with HA and HA-βCD conjugates for 48 h. (c and d) In vitro cell viability of NIH 3T3 and B16F10 cells after incubating with HA and HA-βCD conjugates. (e and f) In vitro cell viability of NIH 3T3 and B16F10 cells after incubating with HA and HA-βCD conjugates. Data are presented as the mean ± SD (n = 4). Statistical significance: ***$p < 0.001$; 'ns' indicates no significance.

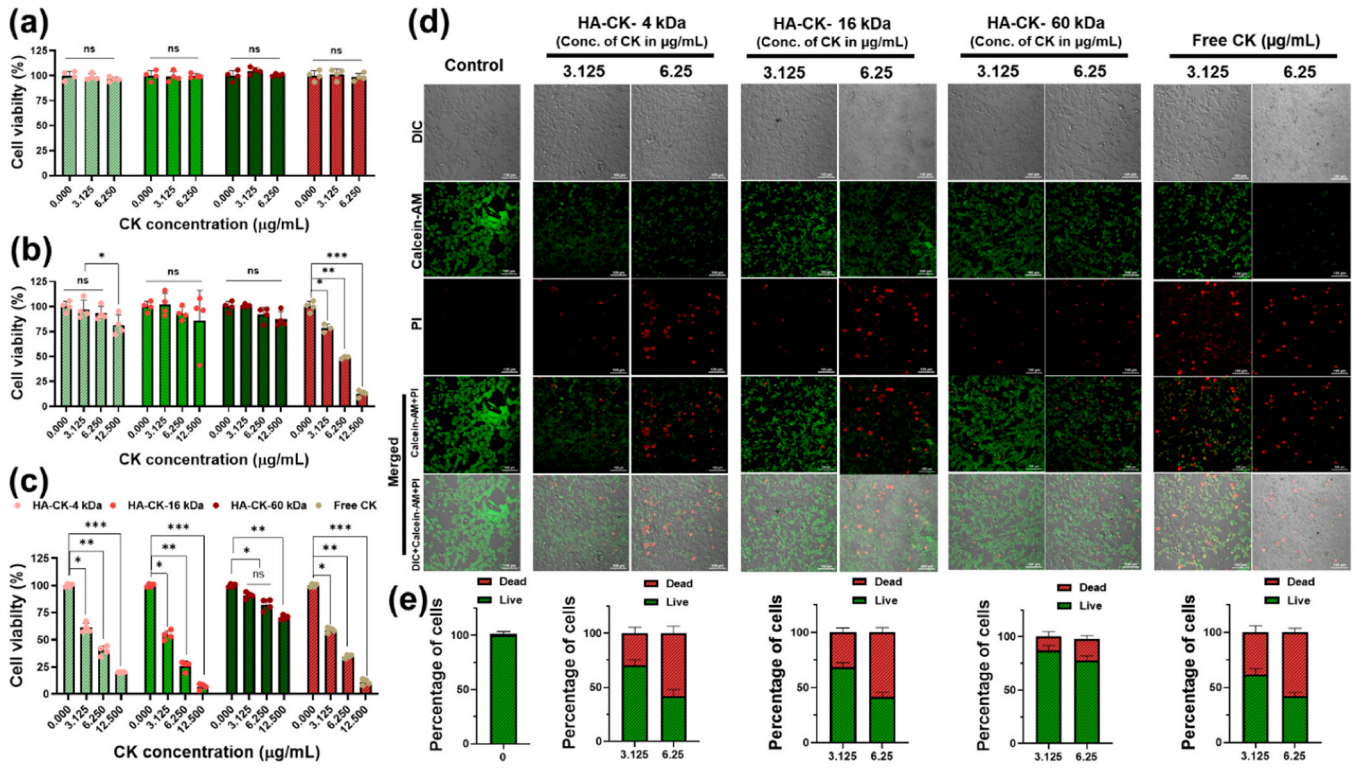

Fig. 5. Cancer cell killing ability of HA-CK conjugates. (a, b, c) In vitro cell killing ability of NIH 3T3, MCF-7 and B16F10 cells after incubation in HA-CK conjugates with different concentration of CK. Free CK was used as control for comparison. Data are presented as the mean ± SD (n = 4). (d) Confocal fluorescent microscopic images of Live/Dead staining in B16F10 cells after incubating with HA-CK conjugates with different concentration of CK. Cells were stained with Calcein-AM (green color, live cells) and PI (red color, dead cells). (e) Quantitative comparison of the percentage of live and dead cells. The percentage of live and dead cells was measured using ImageJ software. Scale bar 100 μm. Statistical significance: *$p < 0.05$; **$p < 0.01$; ***$p < 0.001$; 'ns' indicate no significance.

[44]. Quantification of fluorescence intensity revealed no significant increase in intracellular ROS in HA-βCD conjugate-treated HaCaT cells (Fig. 6**a**). While H_2O_2 (positive control) resulted in an increase in intracellular ROS, the results obtained from HA-CK conjugates were compared to those of the positive control group, indicating the ROS-generating potential of HA-CK conjugates (Fig. 6**b**).

ROS can reportedly mediate autophagy-mediated cell death [45]. ROS generation was also analyzed in B16F10 cells to examine the potential for autophagy-mediated cell death induced by HA-CK conjugates. After internalization of HA-CK conjugates, the released CK stimulated ROS generation in B16F10 cells, with a significant enhancement in ROS levels at 6.25 μg/mL. In contrast, no ROS induction was observed in HA-βCD conjugates treated B16F10 cells (Figs. 6**c** and 6**d**). Notably, among the HA-CK conjugates, HA-CK-60 kDa showed low ROS levels, consistent with previous cytotoxicity results, as higher molecular weight HA requires more time for internalization and induces slower ROS generation. As anticipated, ROS generation was moderate, slightly lower than that in B16F10 cells, and higher than that of HaCaT cells. The distinct levels of ROS generation can be explained by changes in the expression levels of CD44 receptors, which induce the CD44-mediated internalization of HA-CK conjugates. These results collectively suggest that ROS induced by CK in the HA-CK conjugates participate in the induction of autophagy. Microscopic images showed an increase in intracellular ROS with an increase in CK concentration (Fig. 6**e**).

2.7. Effect on apoptotic gene and protein expression analysis

This study elucidates the mechanism underlying mitochondria-dependent apoptotic cell death triggered by HA-CK conjugates in B16F10 cells. The gene expression of both anti-apoptotic and apoptotic proteins in HA-CK conjugates-exposed B16F10 cells was analyzed using semi-quantitative RT-PCR. Cells treated with 3.125 and 6.25 μg/mL of HA-CK conjugates were assessed by RT-PCR (Figs. 7**a** and 7**b**). The study focused on the expression levels of the BAX, Bcl-2, and p53 genes, revealing a significant suppression of Bcl-2 expression and an exciting up-regulation of BAX and p53 in HA-CK conjugate-treated cancer cells compared to control cells.

The enhanced expression of BAX is known to play a key role in the intrinsic pathway, responsible for inducing mitochondrial modifications [46]. A dose-dependent activity was observed, indicating an up-regulation of gene expression with increased exposure time to HA-CK conjugates. The decreased Bcl-2 level suggests that HA-CK conjugates effectively mediate intrinsic apoptotic activity. At each time point, total apoptotic (BAX) and anti-apoptotic genes (Bcl-2) and proteins (caspase-9 and caspase-3) were isolated, revealing expression levels indicative of apoptotic gene expression [47]. A previous report has demonstrated that BAX plays a crucial role in inhibiting the anti-apoptotic function of Bcl-2 [48]. The overexpression of Bcl-2 levels leads to the suppression of cytochrome c release from the mitochondria to the cytoplasm and blocks the caspase activation step of the mitochondrial-mediated intrinsic apoptotic pathway [49].

The current study also examined the expression of p53 in treated cells, revealing a dramatic increase in p53 expression in a time-dependent manner. This observation confirms that the up-regulation of p53 plays a pivotal role in activating apoptosis. Previous research has indicated that apoptotic signaling mediated by p53 generates amino-terminal conformational alterations leading to the release of cytochrome c from mitochondria [50]. Cytochrome c, in turn, facilitates the cleavage of caspases-9 and −3, ultimately leading to apoptotic cell death [51]. In this study, GAPDH served as an internal standard, and its expression level remained unchanged.

The percentage of protein expression levels increased after treatment with HA-CK conjugates compared to that in control B16F10 cells. The caspase-3 expression profile showed up-regulation in B16F10 cells

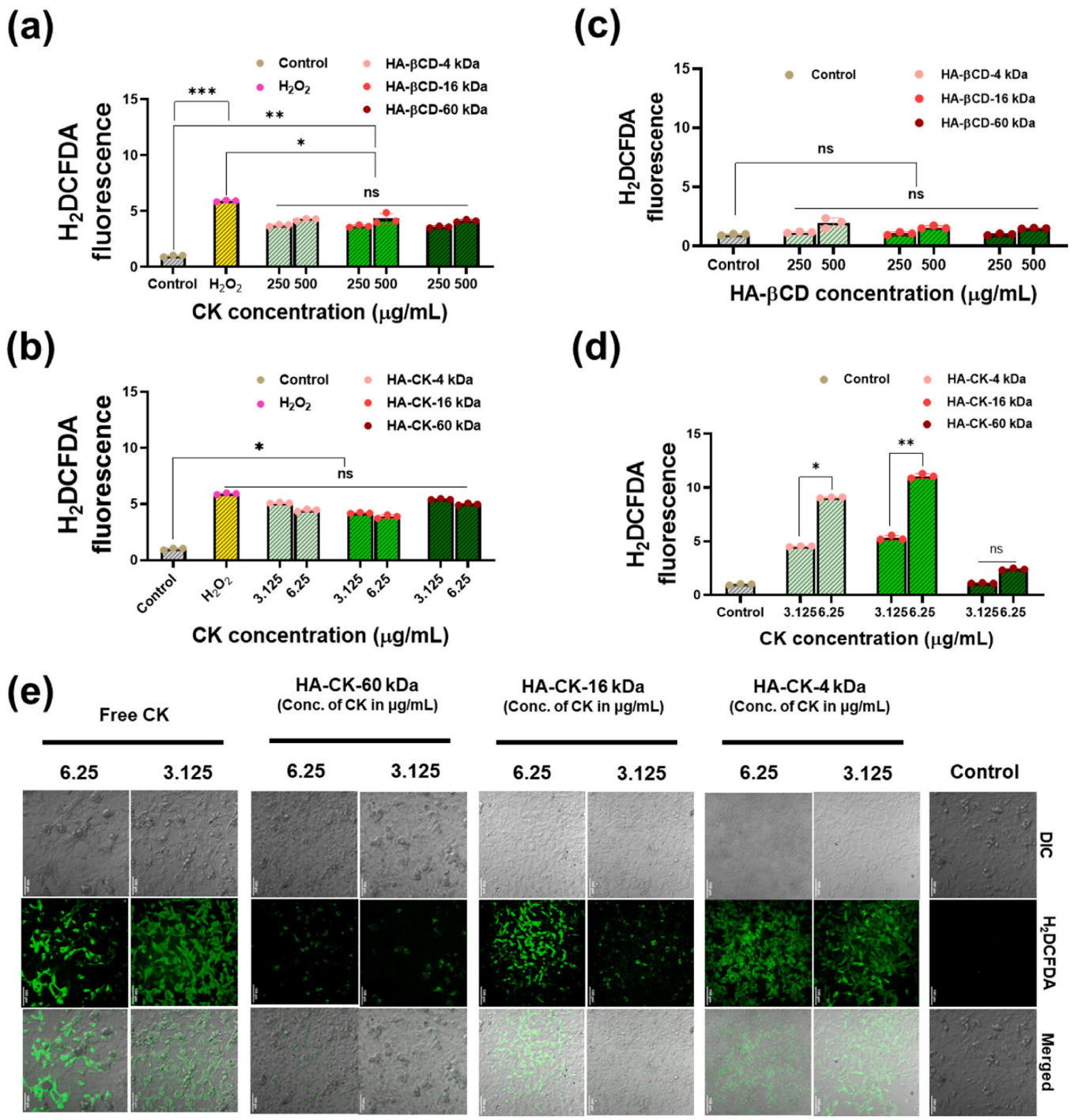

Fig. 6. ROS generation of HA-CK conjugates. The cell-permeable reporter H_2DCFDA was used to quantify ROS production 180 min after the incubation. (a) HaCaT cells were treated with HA-CK conjugates (3.125 and 6.25 μg/mL of CK) for 24 h. (b) B16F10 cells were treated with HA-CK conjugates (3.125 and 6.25 μg/mL of CK) for 24 h. Intracellular ROS accumulation was quantified using microplate reader detection of the oxidized fluorescent H_2DCFDA. Cells treated with 500 μM of H_2O_2 was served as control. The graph shows mean ± SD values of three replicates. (c) CLSM images of H_2DCFDA stained B16F10 cells treated with Free CK and HA-CK conjugates. (d) Quantification of the percentage of H_2DCFDA stained B16F10 cells. The percentage of H_2DCFDA stained B16F10 cells was measured using ImageJ software. The scale bar for images is 100 μm. Statistical significance: *$p < 0.05$; **$p < 0.01$; ***$p < 0.001$; 'ns' indicate no significance.

treated with biogenic HA-CK conjugates. This examination confirms that the up-regulation of caspase-9 triggers the activation of caspase-3. Caspase-3 is a key effector caspase activated through either the death-receptor or mitochondria-mediated pathway [52]. It has been reported that apoptosis mediated by p53 induces the membrane translocation of BAX, which may amplify the apoptotic signal by activating caspase-9 and other downstream caspases, such as caspase-3 [53]. Cytochrome c, acting as a necessary factor for ATP production, also plays a central role in apoptosis [54].

The mechanism behind the cascade activation involves the release of mitochondrial cytochrome c, leading to the subsequent activation of caspase-3 [55]. Caspase-3 then cleaves a variety of substrates, resulting in characteristic morphological changes in the nucleus, DNA fragmentation, and the appearance of the phagocytic marker phosphatidylserine on the cell surface [56]. In summary, the present findings clearly demonstrate the underlying mechanisms and principal mode of cell

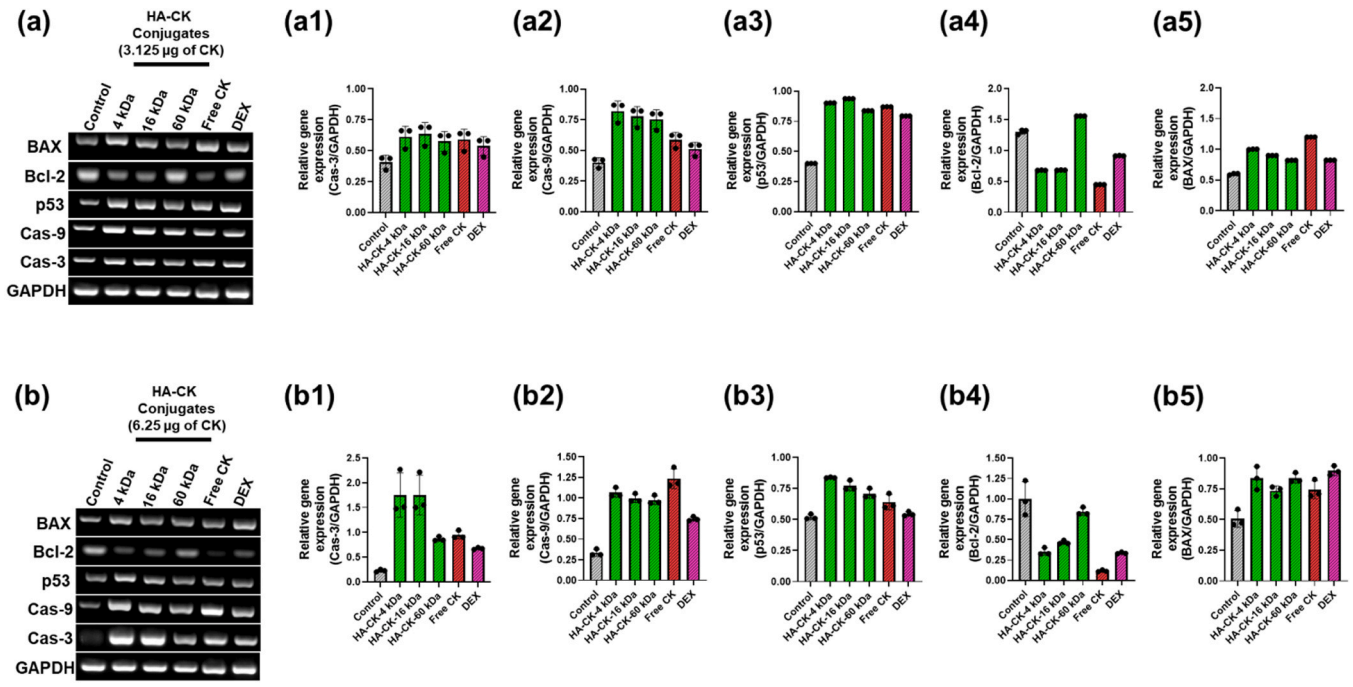

Fig. 7. (**a** and **b**) The semi-quantitative RT-PCR images demonstrates the gene expression changes for BAX, Bcl-2, p53, Cas-9 and Cas-3 of B16F10 cells exposed to HA-CK conjugates with 3.125 and 6.25 g/mL concentration of CK. GAPDH expression was used as a loading control. (**a1-a5** and **b1-b5**) The amounts of the RT-PCR products, quantified using ImageJ, are shown as arbitrary units. Gene expression in each lane was determined by normalizing the intensity of each band to that of GAPDH. Data are plotted as mean ± SD of three independent experiments. Statistical significance: *$p < 0.05$; **$p < 0.01$; ***$p < 0.001$; 'ns' indicate no significance.

death induced by HA-CK conjugates, which involves the intrinsic mitochondrial-mediated apoptosis pathway in B16F10 cells.

2.8. Anti-tumor effects induced by the local therapy in vivo

To assess the therapeutic effects of the injectable hydrogel on mouse melanoma, a melanoma tumor model was established, and the hydrogel

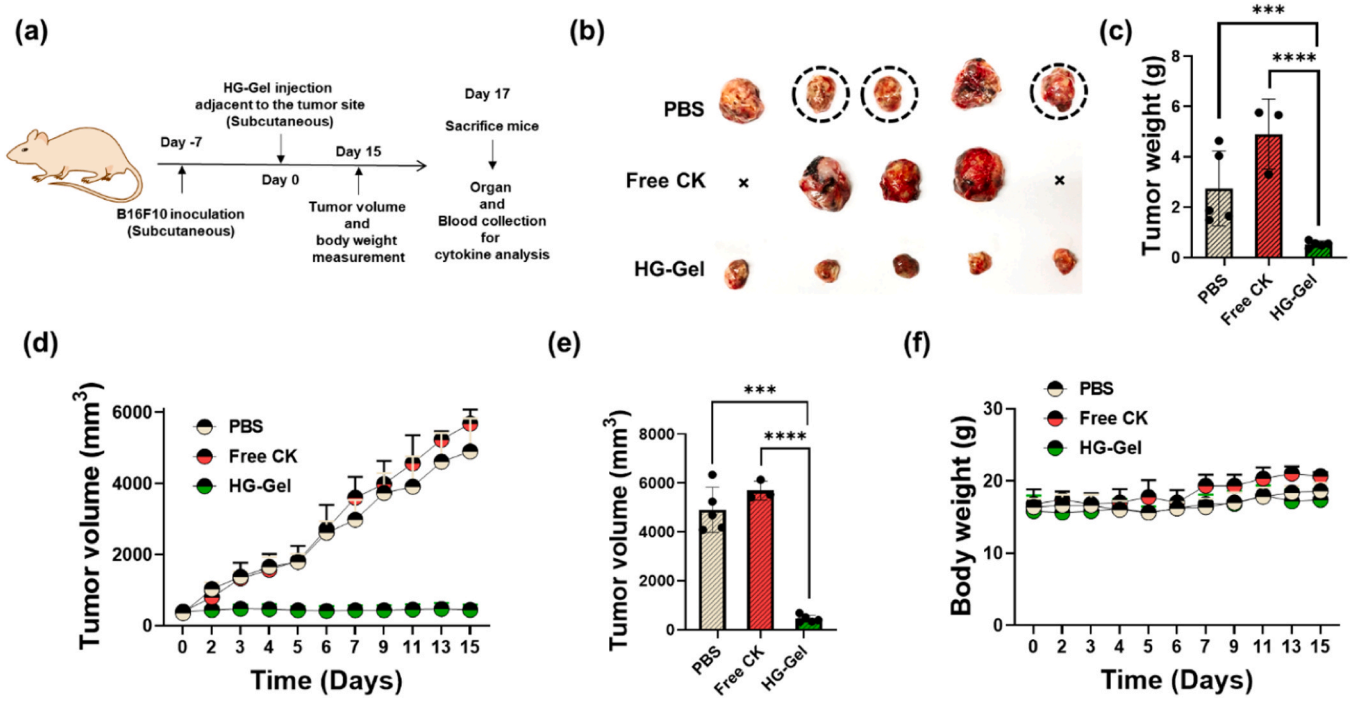

Fig. 8. Anti-tumor effects induced by the local chemotherapy in vivo. (a) The flow chart of the animal experiment. (b) Images of B16F10 tumors treated with different treatments at the end of the experiment (n = 5). The tumors in the PBS mice groups (highlighted by dotted circle) ruptured on the 16th day due to over tumorigenesis. In the CK group, two mice died on the 5th and 6th days, respectively, marked with "×". (c-e) The tumor weight, tumor growth curves and volume of B16F10 tumor-bearing mice models treated with different formulations (n = 5). (f) The body weight of mice treated with different treatments during the experiment (n = 5). Statistical significance: ***$p < 0.001$; ****$p < 0.0001$.

was injected in situ around the tumors. Once the tumor volume reached 200 mm^3, the mice were randomly divided into three groups, each of which received different treatments. After 14 days, the mice were euthanized, and tumor tissues and major organs were extracted for tumor analysis. In addition, blood collection was also carried out to investigate the anti-tumor mechanism (Fig. 8**a**).

To illustrate the therapeutic effects of HG-Gels treatment, a melanoma tumor model was established. The findings demonstrated that, in comparison to CK treatment alone and the PBS group, HG-Gels treatment significantly suppressed tumor growth. As depicted in Fig. 6b-e, the tumors in the CK-only treated group exhibited rapid growth, similar to the PBS group, suggesting that CK alone diffused or metabolized quickly. Interestingly, mice treated with HG-Gels displayed the most pronounced tumor inhibition efficacy compared to the PBS and free CK control groups (Figure S10, Supporting Information). The heightened anti-tumor efficacy of HG-Gels can be attributed to the prolonged delivery of CK to the tumor tissues from the HG-Gel depot, which operates through a diffusion-controlled mechanism. Additionally, the potential delivery of CK through HA-CK conjugates, facilitated by internalization via CD44-mediated specific endocytosis, and triggered burst release of CK by intracellular enzymes, may contribute to the enhanced anti-tumor effects. These results indicate a significantly improved anti-tumor efficiency through localized delivery of triterpenoid saponins from HG-Gels.

Furthermore, monitoring the mice's body weights revealed no apparent systemic toxicity from localized treatment (Fig. 8**f**). Importantly, there was no noticeable weight loss or tissue injury observed in the mice after all treatments, underscoring the high in vivo biocompatibility of HG-Gel-based treatments.

To explore the antitumor effects and systemic toxicity, we collected tumors and major organs (e.g., lung, heart, liver, kidney, and spleen) for histological analysis at the conclusion of the treatment. H&E staining images revealed a dense cancer cell population in the PBS and Free CK groups (Fig. 9a). Notably, the HG-Gels group exhibited a reduced density of cancer cells due to apoptosis induced by the controlled and prolonged release of the anti-cancer drug CK from the hydrogel formulation. This enhanced apoptosis was further validated by the TUNEL assay, which demonstrated the highest apoptosis in the HG-Gels group (Fig. 9**b**). These investigations confirm the prominent anti-tumor potential of HG-gels. Furthermore, the proliferative effect of tumor cells in tumor tissues was examined using Ki67 immunohistochemistry (Figs. 9c and 9d). As a representative marker of tumor cell proliferation and growth, the expression of Ki67 was significantly lower in the HG-Gels group than in the PBS group, suggesting the effective inhibition of tumor growth. H&E staining of major organs revealed no obvious pathological damage (Fig. 9e), indicating no systemic toxicity associated with the HG-Gels formulation.

2.9. *Systemic immune responses induced by HG-Gels*

In the realm of anti-tumor immune responses, inflammation-related cytokines play pivotal roles by finely tuning the cellular functions of immune cells. To investigate inflammatory response to HG-Gels, the concentrations of the various cytokines and apoptosis related genes, including IL-6, IL-8, TNF-α, IFN-γ, BAX, Bcl-2, p53, Cas-9, in the serum were detected using RT-PCR following the terminal stage of anti-tumor analysis. IL-6, IL-8, TNF-α, and IFN-γ, recognized as crucial proinflammatory cytokines in anti-tumor immune responses, orchestrate the commitment, development, and maturation of multiple immune cells. Notably, the HG-Gels treated groups exhibited a significant increase in serum concentrations of TNF-α and IFN-γ compared to both the PBS and

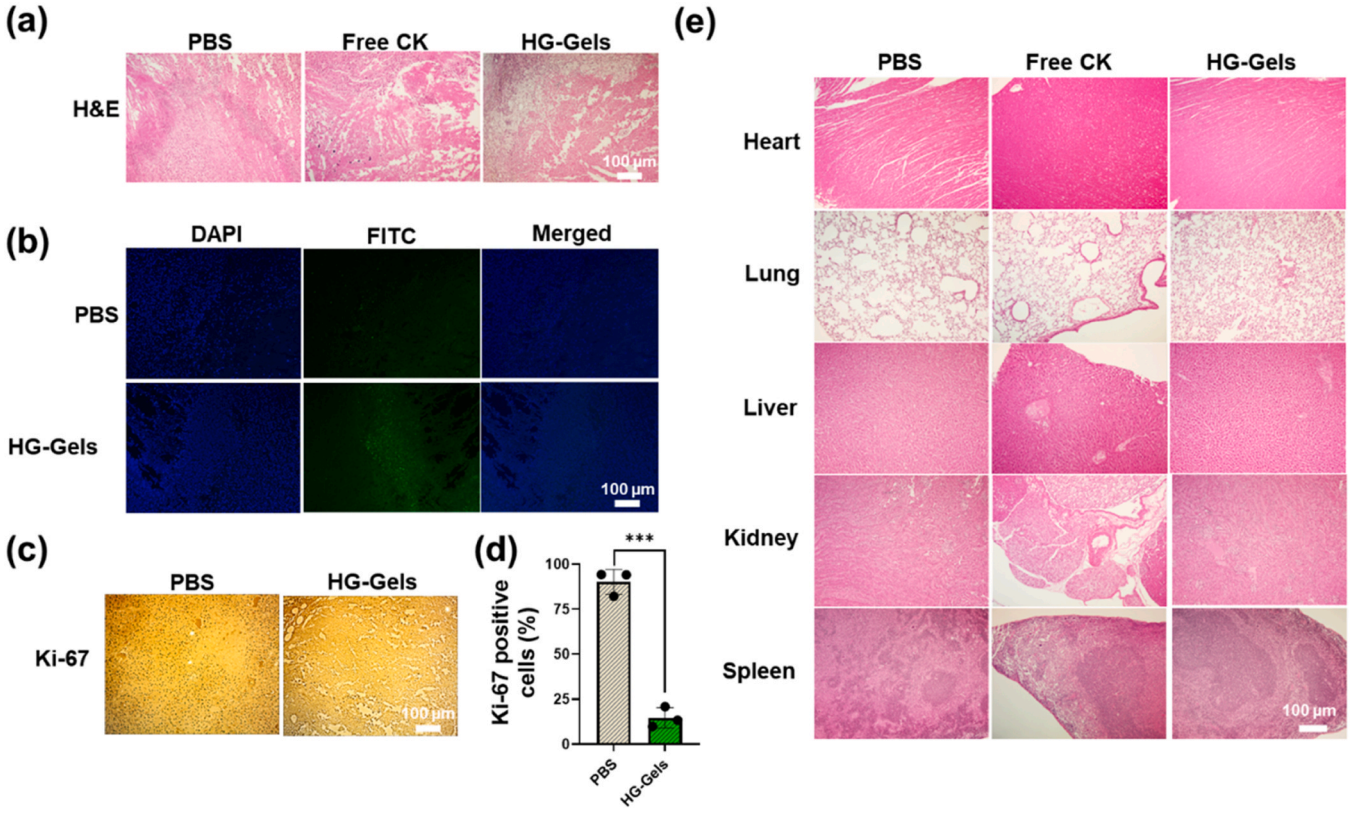

Fig. 9. Histological and immunohistochemical analyses of tumor tissues and major organs. (a) H&E staining images depicting B16F10 tumor tissues in each group (scale bar = 100 μm). (b) TUNEL staining revealed pathological changes in tumor tissues from different groups. Cell nuclei were stained blue (DAPI), and green fluorescence (FITC) indicated apoptotic cells in TUNEL analysis (scale bar = 100 μm). (c and d) Immunohistochemistry showing the expression of the cell proliferation marker, Ki67 protein, in tumor tissues from each group (scale bar = 100 μm). (e) H&E-stained images of major organs with different treatments at the end of the experiment in the B16F10-bearing model (scale bar = 100 μm). Statistical significance is denoted as ***$p<0.001$.

CK groups (Figs. 10**a and** 10**b**). This suggests the optimal effectiveness of HG-Gels in triggering anti-tumor immune responses.

This effectiveness was further manifested in the examination of apoptosis-related genes. The expression of the Bcl-2 gene was significantly reduced, while caspase-3 expression in the HG-Gels treated group increased compared to that in the control group (Figs. 10**c and** 10**d**). This confirms the heightened apoptosis induced by the sustained release of CK from the HG-Gels formulation. In summary, our study reveals that HG-Gels up-regulate proinflammatory cytokines in the serum, concurrently enhancing apoptosis induction. This sheds light on the systemic immune responses induced by the local treatment of HG-Gels in vivo.

Although apoptosis is generally non-immunogenic, treatment-induced modifications and the release of certain molecules can convert this form of cell death into an immunostimulatory event, engaging the immune system and potentially contributing to the therapeutic effects. For instance, during apoptosis, cells can release damage-associated molecular patterns (DAMPs) such as ATP, calreticulin, and High Mobility Group Box 1 (HMGB1) [57]. These molecules act as signals that alert the immune system to the presence of dying cells, leading to an immune response. Additionally, measuring the levels of chemokines (e.g., CCL2, CCL17, and CXCL10) in the tumor microenvironment can further support the evidence of treatment-induced remodeling [58]. As shown in Figure S1 (Supporting Information), both HMGB1 and chemokine CCL17 were downregulated in the HG-Gels treatment group, which inhibited the migration and progression of melanoma. These results support the notion that HG-Gel treatment induces significant remodeling of the tumor immune microenvironment, leading to enhanced anti-tumor immunity.

3. Conclusions

In this study, we aimed to enhance the clinical translatability of triterpenoid saponins by employing a biocompatible and sustained release *in situ* injectable hydrogel for localized delivery of the chemotherapy drug CK. Unlike conventional gel systems, our HG-Gels comprise a naturally derived host polymer conjugate of HA-βCD and a guest polymer conjugate HA-CK. We demonstrated the stability and safety of this delivery system and its potential for clinical applications. The injectable hydrogel system directly induced ROS-mediated cell death in melanoma cells. Furthermore, our strategy of localized CK delivery from HG-Gels demonstrated the highest tumor inhibition efficacy in a mouse model with B16F10 xenografts, without apparent systemic side effects. The enhanced anti-tumor efficacy of HG-Gels is believed to be associated with increased apoptosis induction through the caspase-dependent pathway and the promotion of inflammatory cytokines (IL-6, IL-8, TNF-α, and IFN-γ). Based on these promising results, the localized delivery of the triterpenoid saponin CK using the biodegradable and biocompatible HG-Gel hydrogel presents itself as a highly promising platform for the efficient treatment of cancers, particularly melanoma.

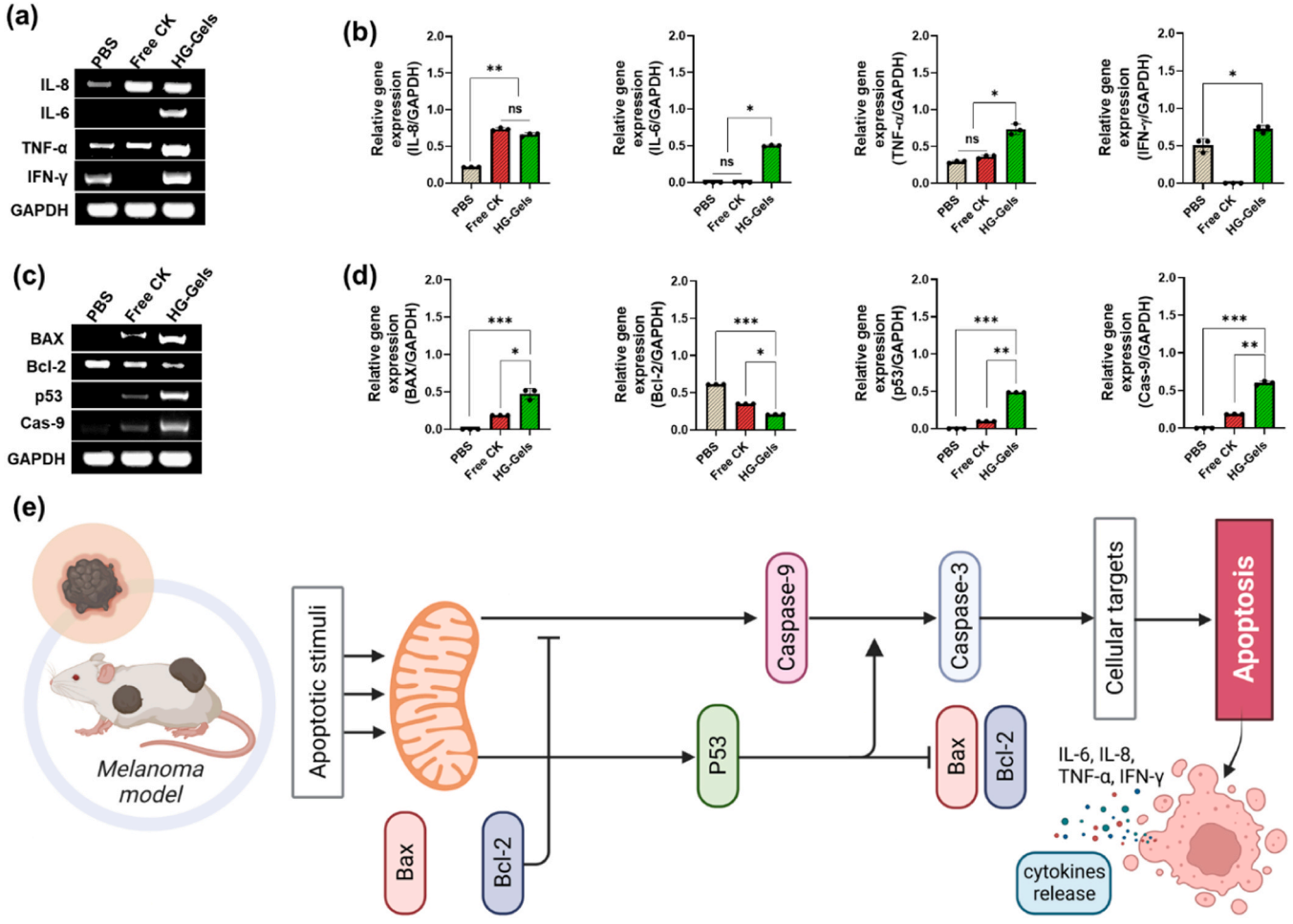

Fig. 10. The expression of proinflammatory cytokines and apoptosis induced gene levels in mouse serum was analyzed using semi-quantitative RT-PCR after treatments. Gene expression in each lane was determined by normalizing the intensity of each band to that of GAPDH. Data are plotted as mean ± SD of three independent experiments. Statistical significance: *p < 0.05; **p < 0.01; ***p < 0.001; 'ns' indicate no significance.

4. Materials and methods

4.1. Synthesis of HA-βCD conjugates

The synthesis route for preparing HA-βCD conjugates is illustrated in the provided Figure S1a, Supporting Information. The conjugation process involved the esterification reaction between the carboxyl group in HA (1 mmol) and the primary hydroxyl group in βCD (0.3 mmol). To initiate the reaction, HA was dissolved in a mixture of formamide and DMF (1:1) at a concentration of 10 wt%, followed by the addition of CDI. The mixture was stirred at room temperature for 30 minutes. Subsequently, βCD was introduced, and the stirring process continued for an additional 48 hours. The resulting reaction mixture was then transferred to cellulose membrane tubes with a molecular weight cutoff (MWCO) of 3500 kDa. Extensive dialysis against deionized water was carried out over a period of three days. Finally, the HA-βCD conjugates were obtained through lyophilization.

4.2. Synthesis of HA-CK conjugates

The synthesis route for preparing HA-CK conjugates is depicted in the provided Figure S1b, Supporting Information. The conjugation process entailed the esterification reaction between the carboxyl group in HA (1 mmol) and the primary hydroxyl group in CK (0.2 mmol). To initiate the reaction, HA was dissolved in a formamide and DMF mixture (1:1) at a concentration of 10 wt%, with the subsequent addition of CDI. The mixture was stirred at room temperature for 30 minutes. Following this, CK dissolved in DMF was introduced, and the stirring process continued for an additional 48 hours. The resulting reaction mixture was then transferred to cellulose membrane tubes with a molecular weight cutoff (MWCO) of 3500 kDa. Extensive dialysis against deionized water was conducted over a period of three days. Ultimately, the HA-βCD conjugates were obtained through lyophilization.

5. Characterization

5.1. NMR

The HA-βCD and HA-CK conjugates were dissolved in D_2O, along with a mixture of D_2O and DMSO-D_6 (1:1), for NMR analysis. Subsequently, 0.75 mL of the prepared samples was transferred into an NMR tube and allowed to cool at room temperature. The NMR spectra were then acquired using spectrometers operating at 400 MHz (JNM-ECZ400S/L1).

5.2. FTIR

The HA-βCD and HA-CK conjugates were prepared, followed by a 48-hour lyophilization process to yield a powder. Subsequently, the obtained powder was compressed with potassium bromide and subjected to analysis using an infrared spectrometer (Spectrum One System by Perkin-Elmer). Additionally, the FTIR spectra of free HA, βCD, and CK were recorded in addition to those of the conjugates.

5.3. Powder XRD

The HG-Gels were prepared and subjected to a 48-hour freeze-drying process to obtain a powdered form. An adequate quantity of the resulting freeze-dried powder was then analyzed using powder X-ray diffraction (D8 Advance by Bruker) at room temperature. The analysis was conducted with the following parameters: a voltage of 40 kV, a current of 240 nm, and a working length spanning from 5° to 40°.

5.4. DSC characterization

The HG-Gels underwent characterization using a differential scanning calorimeter (Q-1000 by TA). The HG-Gels samples were sealed in aluminum pans for testing, with an empty pan serving as the reference. The samples were initially equilibrated at 20 °C and subsequently cooled to −70 °C.

5.5. TGA

The thermal stability of HG-Gels was assessed through thermogravimetric analysis (TGA Q5000 IR / SDT Q600 by TA) with a temperature ramp of 10 °C/min under a dynamic nitrogen flow of 20 mL/min.

5.6. Scanning electron microscopy

Multiple HG-Gels samples were prepared, frozen, and subsequently subjected to freeze-drying. The resulting freeze-dried samples were then sliced into small sections and affixed to SEM stubs. Before examination, a thin layer of gold was applied to the xerogels, and the analysis was carried out using a high-resolution MERLIN microscope (Carl Zeiss).

5.7. Rheological measurements

The viscosity of the HG-Gels as a function of shear rate was measured to investigate the effect of shear-thinning property of the gels. The viscosity of HG-Gels was measured within the shear rate range of 0–50 1/s using a rheometer (Anton Paar QC viscometer). The mechanical tests were carried out to measure the compression modulus of HG-Gels by following the previously reported procedure[37].

5.8. In vitro stability and release test

The stability of HG-Gels was confirmed by incubating them under physiological conditions (pH 7.4, 37 °C) with gentle shaking at 20 rpm. Gels were photographed at several time points. For the in vitro release test, the PBS solution on top of the HG-Gels was removed at predetermined intervals and replaced with an equal volume of fresh PBS. The CK concentration in the PBS was measured following a previously reported procedure[59].

5.9. Hemolytic activity assay

For the hemolytic activity assay, erythrocytes were obtained by centrifuging mouse blood at 3500 rpm for 10 minutes. The acquired erythrocytes were washed three times with PBS, and the purified erythrocytes were subsequently diluted to a final concentration of 10 % v/v. In a 1.5 mL tube, 0.9 mL of the polymer dispersion was combined with 0.1 mL of the erythrocyte suspension. After incubating at 37 °C for 3 hours, all samples underwent centrifugation at 15,000 rpm for 3 minutes. Subsequently, 100 μL of the supernatants were transferred into a new 96-well clear plate, and the absorbance at 541 nm was measured using a microplate reader (BioTek). The positive control consisted of 0.1 % Triton X-100, while PBS served as the negative control.

5.10. In vitro biocompatibility

The cytocompatibility of HG-Gel precursors was assessed using the methyl thiazolyl tetrazolium (MTT) assay against both normal (HaCaT and NIH 3T3) and cancer cells (MCF7 and B16F10 cells). In brief, 96-well plates were seeded with Dulbecco's Modified Eagle Medium (DMEM) or RPMI containing cells (1 × 10^4 cells/well) and incubated at 37 °C with 5 % CO_2 for 24 hours. Subsequently, the medium was replaced with fresh medium, and copolymer solutions of varying concentrations were introduced. PBS treatments served as the negative control. After an additional 24-hour incubation, the copolymer solutions were removed, cells were washed with PBS, and MTT assays were performed by using a microplate reader at 490 nm. Cell viability was

calculated using the formula:

Cell viability (%) = (OD_{sam}/OD_{PBS}) × 100 %, where OD_{sam} and OD_{PBS} represent the absorbencies of the cells treated with polymer and PBS, respectively.

5.11. Cytotoxicity measurement in vitro

The cytotoxicity of HA-CK conjugates was evaluated using the MTT assay against various normal and cancer cells. In a nutshell, 96-well plates were seeded with cells in RPMI or DMEM (5 × 10^3 cells/well) and incubated at 37 °C with 5 % CO_2 for 24 hours. Subsequently, the medium was replaced with fresh medium containing varying concentrations of drugs (CK: 12.5, 6.25, and 3.125 μg/mL), followed by an additional 48-hour incubation period. Following this, cell viability was assessed using the MTT assay, and the viability was calculated using the formula used in the previous section.

Additionally, a live/dead assay was conducted to assess cell viability. Following a 24-hour incubation, HA-CK conjugates were washed with 10 mM phosphate-buffered saline (PBS) at pH 7.4 and then stained using a live/dead cell staining kit (BioVision, Milpitas, CA). Fluorescent images were captured using a Nikon Confocal A1R fluorescence microscope. The percentage of live and dead cells was quantified using ImageJ software (NIH, Bethesda, MD).

5.12. ROS generation in vitro

The estimation of reactive oxygen species (ROS) was conducted using the cell-permeant 2′,7′-dichlorodihydrofluorescein diacetate (H_2DCF-DA), which permeates the cell and reacts with reactive oxygen to produce a green fluorescent compound called dichlorofluorescein (DCF)[60]. The ROS generation in B16F10 cells was visualized using a Nikon Confocal A1R fluorescence microscope. A stock solution of H_2DCF-DA (10 mM) was initially prepared in methanol and further diluted with culture medium to a working concentration of 100 μM. Cells were treated with HA-CK conjugates (CK concentrations: 6.25 and 3.125 μg/mL) for 12 hours. Subsequently, the cells were washed with ice-cold Hanks balanced salt solution (HBSS) and incubated with 100 μM (working solution) of H_2DCF-DA for 30 minutes at 37 °C. Following this, the cells were lysed with alkaline solutions, and the fluorescence intensity was measured at an excitation of 485 nm and emission at 520 nm using a BioTek plate reader. Cells treated with 1 % H_2O_2 for 6 hours were used as positive controls.

5.13. Semi-quantitative RT-PCR analysis for apoptotic gene expression

Alterations in the expression profiles of BAX, Bcl-2, p53, Cas-9, and Cas-3 were identified through RT-PCR analysis. Total RNA from B16F10 cells treated with HA-CK conjugates was isolated using TriZol reagent. Briefly, cDNA was synthesized using a cDNA synthesis kit and then amplified according to the manufacturer's protocols in a 25 mL reaction mixture, including random primer pairs (1.0 mL), buffer (5.0 mL), cDNA (2.0 mg), 25 mM/L MgCl (3.0 mL), 10 mM/L dNTPs (1.0 mL), and Taq polymerase (2.5 U). Semi-quantitative RT-PCR amplification involved denaturation at 94 °C for 1 minute, primer annealing at 57 °C for 45 seconds, and extension at 72 °C for 45 seconds, totaling 30 cycles, followed by terminal extension at 72 °C for 10 minutes. The primer sequences for GAPDH, BAX, Bcl-2, p53, Cas-9, and Cas-3 are provided in Table S3, Supporting Information, with GAPDH serving as the internal reference.

5.14. In vivo gelation of HG-Gels

For in situ gelation, 200 μL of HG-Gels was injected into the dorsal region of BALB/c mice. The mice were subsequently euthanized, and the gels were photographed 30 minutes post-injection.

5.15. Anti-tumor efficacy of the drug-loaded hydrogels in vivo

All animal experiments were performed in accordance with the guidelines of the Institutional Animal Experiment Committee of Kyung Hee University. The Institutional Committees of Kyung Hee University approved our experiments (approval number: KHU-22–216). The in vivo anti-tumor efficacy of HG-Gels was assessed using a B16F10 xenograft model in female BALB/c mice (6 weeks old). In brief, a suspension of B16F10 cells (0.1 mL PBS containing 1 × 10^6 cells per mouse) was subcutaneously injected into the armpit of the right limb, leading to tumor formation approximately one week later. When the tumor volume reached about 100 mm^3, mice bearing B16F10 tumors were randomly divided into six groups (5 mice/group), including a PBS control group, a free CK group, and HG-Gels groups (5 mg of CK/kg mice). Treatment involved a single injection of free CK or HG-Gels (CK: 5 mg/kg, 0.2 mL per mouse). To assess therapeutic efficacy and safety, tumor volume and body weight were recorded every other day. Tumor volume was calculated using the formula: $V = Long\ \text{diameter} \times Wide\ diameter^2/2$. After the experiment, the mice were anesthetized, and tumor tissues and major organs (heart, liver, spleen, lung, and kidney) were collected, immersed in 10 % neutrally buffered formaldehyde, and embedded in paraffin. Paraffin-embedded tumor tissue samples were sliced and stained with H&E, TUNEL, and Ki67 for histopathological analysis. In addition, the major organs were stained with H&E to investigate the safety of the organs. Furthermore, blood from the mice also drawn to investigate proinflammatory (IFN, TNF, IL-6 and IL-8) and apoptosis-related genes (Cas-9, p53, Bcl-2, and BAX) in the tumor-bearing mice using RT-PCR analysis, as described earlier, with three independent samples tested for each data point.

5.16. Statistical analysis

All experiments were conducted in triplicate, unless otherwise specified. Data analysis was performed using GraphPad Prism 9.0. Student's t-test or one-way ANOVA with Tukey's post hoc test was employed for comparisons between two groups or multiple groups, respectively. Results are presented as mean ± SD. Significance levels were denoted as follows: *$p < 0.05$, **$p < 0.01$, ***$p < 0.001$.

CRediT authorship contribution statement

João Conde: Writing – review & editing, Writing – original draft, Validation, Supervision, Project administration, Investigation, Funding acquisition, Formal analysis, Conceptualization. **Vinothini Boopathi:** Investigation, Writing – review & editing. **Thavasyappan Thambi:** Writing – review & editing, Writing – original draft, Visualization, Validation, Supervision, Resources, Project administration, Investigation, Funding acquisition, Formal analysis, Conceptualization. **Zelika Mega Ramadhania:** Writing – review & editing, Writing – original draft, Investigation. **Jinnatun Nahar:** Writing – review & editing, Writing – original draft, Investigation. **Ramya Mathiyalagan:** Writing – review & editing, Writing – original draft, Methodology, Investigation, Data curation. **Mohananpriya Murugesan:** Writing – review & editing, Writing – original draft, Investigation. **Panchanathan Manivasagan:** Writing – review & editing, Writing – original draft, Investigation. **Eue-Soon Jang:** Writing – review & editing, Writing – original draft, Supervision, Investigation. **Deok Chun Yang:** Writing – review & editing, Writing – original draft, Investigation.

Declaration of Competing Interest

J.C. is a co-founder and shareholder of TargTex S.A. – Targeted therapeutics for Glioblastoma Multiforme. J.C. is a member of the Global Burden Disease (GBD) consortium of the Institute for Health Metrics and Evaluation (IHME), University of Washington (US) and is in the Scientific Advisory board of Vector Bioscience Cambridge. The other authors

declare no conflicts of interest.

Data Availability

Data will be made available on request.

Acknowledgements

This work was supported by a National Research Foundation of Korea (NRF) grant funded by the Korean government (MSIT) (NRF-2020R1I1A1A01070867, R.M.; NRF-2023R1A2C1005904, T.T.; 2016R1D1A3B0201175615, E. -S.; NRF-2022R1I1A1A01068693, P. M.;). The Ministry of Health and Welfare (HP23C0260), and the Innovative Human Resource Development for Local Intellectualization Program (IITP-2024–2020-0-01612) through the Institute of Information & Communications Technology Planning & Evaluation (IITP) funded by the Ministry of Science and ICT (MSIT), Korea. J.C. acknowledges the European Research Council (ERC) under the European Union's Horizon 2020 Research and Innovation Program (ERC-StG-2019-848325).

Appendix A. Supporting information

Supplementary data associated with this article can be found in the online version at doi:10.1016/j.mser.2024.100824.

References

[1] R. Zhong, S. Talebian, B.B. Mendes, G. Wallace, R. Langer, J. Conde, J. Shi, Nat. Mater. 22 (2023) 818.
[2] (a) P. Bertsch, M. Diba, D.J. Mooney, S.C.G. Leeuwenburgh, Chem. Rev. 123 (2023) 834;
(b) J.E. Mealy, J.J. Chung, H.-H. Jeong, D. Issadore, D. Lee, P. Atluri, J.A. Burdick, Adv. Mater. 30 (2018) 1705912;
(c) L.J. Eggermont, Z.J. Rogers, T. Colombani, A. Memic, S.A. Bencherif, Trends Biotechnol. 38 (2020) 418.
[3] (a) D. Chimene, R. Kaunas, A.K. Gaharwar, Adv. Mater. 32 (2020) 1902026;
(b) L. Hao, H. Mao, Biomater. Sci. 11 (2023) 6384;
(c) A.H. Milani, L.A. Fielding, P. Greensmith, B.R. Saunders, D.J. Adlam, A. J. Freemont, J.A. Hoyland, N.W. Hodson, M.A. Elsawy, A.F. Miller, L.P.D. Ratcliffe, O.O. Mykhaylyk, S.P. Armes, Chem. Mater. 29 (2017) 3100.
[4] (a) Y. Hu, Z. Du, X. Deng, T. Wang, Z. Yang, W. Zhou, C. Wang, Macromolecules 49 (2016) 5660;
(b) Q. Wang, Y. Zhang, Y. Ma, M. Wang, G. Pan, Mater. Today Bio 20 (2023) 100640.
[5] X. Yu, Y. Wang, H. Zhang, Z. Li, Y. Zheng, X. Fan, Y. Lv, X. Zhang, T. Liu, Chem. Mater. 35 (2023) 9287.
[6] C. Li, N. Schramma, Z. Wang, N.F. Qari, M. Jalaal, M.I. Latz, S. Cai, Sci. Adv. 9 (2023) eadi8643.
[7] C.B. Rodell, N.N. Dusaj, C.B. Highley, J.A. Burdick, Adv. Mater. 28 (2016) 8419.
[8] X. Du, J. Zhou, J. Shi, B. Xu, Chem. Rev. 115 (2015) 13165.
[9] Y. Tang, M. Hu, F. Tang, R. Huang, H. Wang, D. Wu, P. Lan, Bioact. Mater. 15 (2022) 44.
[10] M.H. Chen, L.L. Wang, J.J. Chung, Y.-H. Kim, P. Atluri, J.A. Burdick, ACS Biomater. Sci. Eng. 3 (2017) 3146.
[11] (a) B. Miller, A. Hansrisuk, C.B. Highley, S.R. Caliari, bioRxiv 2021 (2021), 02.26.430926;
(b) M. Jain, B.P. Nowak, B.J. Ravoo, ChemNanoMat 8 (2022) e202200077.
[12] (a) G. Sinawang, M. Osaki, Y. Takashima, H. Yamaguchi, A. Harada, Chem. Commun. 56 (2020) 4381;
(b) Z. Wei, J.H. Yang, J. Zhou, F. Xu, M. Zrínyi, P.H. Dussault, Y. Osada, Y. M. Chen, Chem. Soc. Rev. 43 (2014) 8114.
[13] Y.-M. Zhang, N.-Y. Zhang, K. Xiao, Q. Yu, Y. Liu, Angew. Chem. Int. Ed. 57 (2018) 8649.
[14] (a) W. Zhang, Y.-M. Zhang, S.-H. Li, Y.-L. Cui, J. Yu, Y. Liu, Angew. Chem. Int. Ed. 55 (2016) 11452;
(b) J. Krämer, L.M. Grimm, C. Zhong, M. Hirtz, F. Biedermann, Nat. Commun. 14 (2023) 518.
[15] J.-J. Li, Y. Hu, B. Hu, W. Wang, H. Xu, X.-Y. Hu, F. Ding, H.-B. Li, K.-R. Wang, X. Zhang, D.-S. Guo, Nat. Commun. 13 (2022) 6279.
[16] S. Wüpper, K. Lüersen, G. Rimbach, Biomolecules 11 (2021).
[17] A. Gonzalez Pereira, M. Carpena, P. García Oliveira, J.C. Mejuto, M.A. Prieto, J. Simal Gandara, Int J. Mol. Sci. 22 (2021).
[18] A.C. Paiva-Santos, L. Ferreira, D. Peixoto, F. Silva, M.J. Soares, M. Zeinali, H. Zafar, F. Mascarenhas-Melo, F. Raza, P.G. Mazzola, F. Veiga, Colloids Surf. B: Biointerfaces 218 (2022) 112758.
[19] M. Hashemi, M.A. Zandieh, Y. Talebi, P. Rahmanian, S.S. Shafiee, M.M. Nejad, R. Babaei, F.H. Sadi, R. Rajabi, Z.O. Abkenar, S. Rezaei, J. Ren, N. Nabavi, R. Khorrami, M. Rashidi, K. Hushmandi, M. Entezari, A. Taheriazam, Biomed. Pharmacother. 160 (2023) 114392.
[20] X. Song, Y. Wen, J.-l Zhu, F. Zhao, Z.-X. Zhang, J. Li, Biomacromolecules 17 (2016) 3957.
[21] R. Namgung, Y. Mi Lee, J. Kim, Y. Jang, B.-H. Lee, I.-S. Kim, P. Sokkar, Y.M. Rhee, A.S. Hoffman, W.J. Kim, Nat. Commun. 5 (2014) 3702.
[22] Z. Wei, S. Gerecht, Biomaterials 185 (2018) 86.
[23] T. Guan, J. Li, C. Chen, Y. Liu, Adv. Sci. (Weinh.) 9 (2022) e2104165.
[24] J.C.F. NA, L. Pirson, H. Edelberg, M. M. L, C. Loira-Pastoriza, V. Preat, Y. Larondelle, C.M. André, Molecules (2017) 22.
[25] P.D. Cárdenas, A. Almeida, S. Bak, Front. Plant Sci. 10 (2019).
[26] V.T. Nguyen, N.T. Tung, T.D. Cuong, T.M. Hung, J.A. Kim, M.H. Woo, J.S. Choi, J.-H. Lee, B.S. Min, Phytochem. Lett. 12 (2015) 69.
[27] M. Murugesan, R. Mathiyalagan, V. Boopathi, B.M. Kong, S.-K. Choi, C.-S. Lee, D. C. Yang, S.C. Kang, T. Thambi, Nanomaterials 12 (2022) 3427.
[28] M. Malík, J. Velechovský, P. Tlustoš, Fitoterapia 151 (2021) 104845.
[29] T. Thambi, V.H. Giang Phan, S.H. Kim, T.M. Duy Le, H.T.T. Duong, D.S. Lee, Biomater. Sci. 7 (2019) 5424.
[30] L. Chen, Y. Meng, Q. Sun, Z. Zhang, X. Guo, X. Sheng, G. Tai, H. Cheng, Y. Zhou, Cell Death Dis. 7 (2016) e2334.
[31] M. Kong, X. Chen, H. Park, Carbohydr. Polym. 83 (2011) 462.
[32] G. Giubertoni, G.H. Koenderink, H.J. Bakker, J. Phys. Chem. A 123 (2019) 8220.
[33] T. Uyar, Y. Nur, J. Hacaloglu, F. Besenbacher, Nanotechnology 20 (2009) 125703.
[34] W. Li, L. Ran, F. Liu, R. Hou, W. Zhao, Y. Li, C. Wang, J. Dong, Molecules 24 (2019) 4487.
[35] N.C. Pan, G.T. Bersaneti, S. Mali, M.A.P.C. Celligoi, Braz. Arch. Biol. Technol. 63 (2020).
[36] A. García, D. Leonardi, M.O. Salazar, M.C. Lamas, PLOS ONE 9 (2014) e88234.
[37] V.H.G. Phan, H.-S. Duong, Q.-G.T. Le, G. Janarthanan, S. Vijayavenkataraman, H.-N.H. Nguyen, B.-P.T. Nguyen, P. Manivasagan, E.-S. Jang, Y. Li, T. Thambi, J. Nanobiotechnol. 21 (2023) 405.
[38] N. Marangoci, M. Mares, M. Silion, A. Fifere, C. Varganici, A. Nicolescu, C. Deleanu, A. Coroaba, M. Pinteala, B.C. Simionescu, Results Pharma Sci. 1 (2011) 27.
[39] (a) B.-P. Jiang, L. Zhang, Y. Zhu, X.-C. Shen, S.-C. Ji, X.-Y. Tan, L. Cheng, H. Liang, J. Mater. Chem. B 3 (2015) 3767;
(b) K.M. Lopez, S. Ravula, R.L. Pérez, C.E. Ayala, J.N. Losso, M.E. Janes, I. M. Warner, ACS Omega 5 (2020) 4125.
[40] (a) N. Gull, S.M. Khan, M.T. Zahid Butt, S. Khalid, M. Shafiq, A. Islam, S. Asim, S. Hafeez, R.U. Khan, RSC Adv. 9 (2019) 31078;
(b) Y.-C. Huang, Z.-H. Liu, C.-Y. Kuo, J.-P. Chen, Int. J. Mol. Sci. 23 (2022) 6177;
(c) L. Wang, C. Lu, H. Liu, S. Lin, K. Nan, H. Chen, L. Li, RSC Adv. 6 (2016) 1194.
[41] A. Mero, M. Campisi, Polymers 6 (2014) 346.
[42] H. Xiao, R. Qi, S. Liu, X. Hu, T. Duan, Y. Zheng, Y. Huang, X. Jing, Biomaterials 32 (2011) 7732.
[43] L. Teng, Z. Shao, Q. Bai, X. Zhang, Y.-S. He, J. Lu, D. Zou, C. Feng, C.-M. Dong, Adv. Funct. Mater. 31 (2021) 2105628.
[44] D. Shao, Z. Gao, Y. Zhao, M. Fan, X. Zhao, Q. Wei, M. Pan, B. Ma, Int. J. Mol. Sci. 24 (2023) 1070.
[45] A.D. Kim, K.A. Kang, H.S. Kim, D.H. Kim, Y.H. Choi, S.J. Lee, H.S. Kim, J.W. Hyun, Cell Death Dis. 4 (2013) e750.
[46] H.M. Berens, K.L. Tyler, J. Virol. 85 (2011) 3858.
[47] P. Hussar, Encyclopedia 2 (2022) 1624.
[48] S. Qian, Z. Wei, W. Yang, J. Huang, Y. Yang, J. Wang, Front Oncol. 12 (2022) 985363.
[49] H. Kalkavan, D.R. Green, Cell Death Differ. 25 (2018) 46.
[50] N. Kanipandian, D. Li, S. Kannan, Biotechnol. Rep. 23 (2019) e00339.
[51] C. Garrido, L. Galluzzi, M. Brunet, P.E. Puig, C. Didelot, G. Kroemer, Cell Death Differ. 13 (2006) 1423.
[52] S. McComb, P.K. Chan, A. Guinot, H. Hartmannsdottir, S. Jenni, M.P. Dobay, J.-P. Bourquin, B.C. Bornhauser, Sci. Adv. 5 (2019) eaau9433.
[53] J. Wang, W. Guo, H. Zhou, N. Luo, C. Nie, X. Zhao, Z. Yuan, X. Liu, Y. Wei, Oncotarget 6 (2015) 17192.
[54] J. Wan, H.A. Kalpage, A. Vaishnav, J. Liu, I. Lee, G. Mahapatra, A.A. Turner, M. P. Zurek, Q. Ji, C.T. Moraes, M.A. Recanati, L.I. Grossman, A.R. Salomon, B.F. P. Edwards, M. Hüttemann, Sci. Rep. 9 (2019) 15815.
[55] C.A. Elena-Real, A. Díaz-Quintana, K. González-Arzola, A. Velázquez-Campoy, M. Orzáez, A. López-Rivas, S. Gil-Caballero, M. De la Rosa, I. Díaz-Moreno, Cell Death Dis. 9 (2018) 365.
[56] L. Galluzzi, I. Vitale, S.A. Aaronson, J.M. Abrams, D. Adam, P. Agostinis, E. S. Alnemri, L. Altucci, I. Amelio, D.W. Andrews, M. Annicchiarico-Petruzzelli, A. V. Antonov, E. Arama, E.H. Baehrecke, N.A. Barlev, N.G. Bazan, F. Bernassola, M.J. M. Bertrand, K. Bianchi, M.V. Blagosklonny, K. Blomgren, C. Borner, P. Boya, C. Brenner, M. Campanella, E. Candi, D. Carmona-Gutierrez, F. Cecconi, F.K. M. Chan, N.S. Chandel, E.H. Cheng, J.E. Chipuk, J.A. Cidlowski, A. Ciechanover, G. M. Cohen, M. Conrad, J.R. Cubillos-Ruiz, P.E. Czabotar, V. D'Angiolella, T. M. Dawson, V.L. Dawson, V. De Laurenzi, R. De Maria, K.-M. Debatin, R. J. DeBerardinis, M. Deshmukh, N. Di Daniele, F. Di Virgilio, V.M. Dixit, S.J. Dixon, C.S. Duckett, B.D. Dynlacht, W.S. El-Deiry, J.W. Elrod, G.M. Fimia, S. Fulda, A. J. García-Sáez, A.D. Garg, C. Garrido, E. Gavathiotis, P. Golstein, E. Gottlieb, D. R. Green, L.A. Greene, H. Gronemeyer, A. Gross, G. Hajnoczky, J.M. Hardwick, I. S. Harris, M.O. Hengartner, C. Hetz, H. Ichijo, M. Jäättelä, B. Joseph, P.J. Jost, P. P. Juin, W.J. Kaiser, M. Karin, T. Kaufmann, O. Kepp, A. Kimchi, R.N. Kitsis, D. J. Klionsky, R.A. Knight, S. Kumar, S.W. Lee, J.J. Lemasters, B. Levine, A. Linkermann, S.A. Lipton, R.A. Lockshin, C. López-Otín, S.W. Lowe, T. Luedde, E. Lugli, M. MacFarlane, F. Madeo, M. Malewicz, W. Malorni, G. Manic, J.-

C. Marine, S.J. Martin, J.-C. Martinou, J.P. Medema, P. Mehlen, P. Meier, S. Melino, E.A. Miao, J.D. Molkentin, U.M. Moll, C. Muñoz-Pinedo, S. Nagata, G. Nuñez, A. Oberst, M. Oren, M. Overholtzer, M. Pagano, T. Panaretakis, M. Pasparakis, J.M. Penninger, D.M. Pereira, S. Pervaiz, M.E. Peter, M. Piacentini, P. Pinton, J.H.M. Prehn, H. Puthalakath, G.A. Rabinovich, M. Rehm, R. Rizzuto, C. M.P. Rodrigues, D.C. Rubinsztein, T. Rudel, K.M. Ryan, E. Sayan, L. Scorrano, F. Shao, Y. Shi, J. Silke, H.-U. Simon, A. Sistigu, B.R. Stockwell, A. Strasser, G. Szabadkai, S.W.G. Tait, D. Tang, N. Tavernarakis, A. Thorburn, Y. Tsujimoto, B. Turk, T. Vanden Berghe, P. Vandenabeele, M.G. Vander Heiden, A. Villunger, H. W. Virgin, K.H. Vousden, D. Vucic, E.F. Wagner, H. Walczak, D. Wallach, Y. Wang, J.A. Wells, W. Wood, J. Yuan, Z. Zakeri, B. Zhivotovsky, L. Zitvogel, G. Melino, G. Kroemer, Cell Death Differ. 25 (2018) 486.

[57] A. Murao, M. Aziz, H. Wang, M. Brenner, P. Wang, Apoptosis 26 (2021) 152.

[58] A.A. Bhat, S. Nisar, M. Singh, B. Ashraf, T. Masoodi, C.P. Prasad, A. Sharma, S. Maacha, T. Karedath, S. Hashem, S.B. Yasin, P. Bagga, R. Reddy, M.P. Frennaux, S. Uddin, P. Dhawan, M. Haris, M.A. Macha, Cancer Commun. (Lond.) 42 (2022) 689.

[59] J. Zhang, J. Zhou, Q. Yuan, C. Zhan, Z. Shang, Q. Gu, J. Zhang, G. Fu, W. Hu, J. Ginseng Res. 45 (2021) 228.

[60] M.J. Reiniers, R.F. van Golen, S. Bonnet, M. Broekgaarden, T.M. van Gulik, M. R. Egmond, M. Heger, Anal. Chem. 89 (2017) 3853.

Thavasyappan Thambi is currently working as a Research Professor at the Graduate School of Biotechnology, Kyung Hee University in South Korea. He received his Ph.D. degree from Sungkyunkwan University, working in the field of microenvironment-specific polymeric nanoparticles for imaging and therapy of intractable diseases, and was trained in the Department of Bioengineering, Hanyang University, South Korea. His research focuses on the development of smart hydrogels for cancer therapy and tissue engineering applications. Thus far, he has authored 80+ publications that have been cited over 4300 times, with an H-index of 40. He has been listed in the world's top 2 % scientists list by Stanford University for the past three years.

João Conde is a Group Leader, Professor and Vice-Dean for Research at NOVA Medical School, Universidade NOVA de Lisboa. In 2014, he received his PhD in Biology with a specialization in NanoBiotechnology from the Universidade NOVA de Lisboa and the Universidad de Zaragoza for the development of multifunctional gold nanoparticles for gene silencing. Following that, he was a Marie Curie Fellow at the Massachusetts Institute of Technology, Harvard-MIT Division for Health Sciences and Technology, and Queen Mary University of London's School of Engineering and Materials Science. The main focus of his research is the use of Cancer Nanotechnology for Precision Medicine to tackle crucial medical problems involved in the development of novel and highly effective diagnostic and therapeutic platforms for cancer. In 2019, he won an ERC Starting Grant from the European Research Council to build a genetic biobarcode for profiling breast cancer heterogeneity. He is also a co-founder of the biotech company TargTex, Targeted Therapeutics for Glioblastoma Multiforme. Since 2020, he has been a part of the Global Burden of Disease (GBD) Consortium of the Institute for Health Metrics and Evaluation (IHME), University of Washington. In 2023, he partnered with Vector Bioscience Cambridge and AstraZeneca to develop RNA-based cancer therapies from the European Innovation Council Transition. In 2023, was elected for the Scientific Advisory Board of FCT: Fundação para a Ciência e a Tecnologia. He has authored more than 120 publications that have been cited nearly 12000 times, with an H-index of 54. He was awarded several international awards, including the 2023 and 2022 World's Top 2 % Scientists list by Stanford University, the Nanomaterials 2020 Young Investigator Award, the 2021 Biomaterials Science Emerging Investigator, the Top 2 % Most Cited in Nanoscience/Nanotechnology from PLOS Biology, the Wellcome Image Awards 2017, the Nano-Micro Letters Researcher Award, and the National Cancer Institute Image Award.